

# The SRG/eROSITA All-Sky Survey

## Constraints on Ultra-light Axion Dark Matter through Galaxy Cluster Number Counts

S. Zelmer<sup>1</sup>, E. Artis<sup>1</sup>, E. Bulbul<sup>1</sup>, S. Grandis<sup>2</sup>, V. Ghirardini<sup>3</sup>, A. von der Linden<sup>4,1</sup>, Y. E. Bahar<sup>1</sup>, F. Balzer<sup>1</sup>, M. Brüggen<sup>5</sup>, I. Chiu<sup>6</sup>, N. Clerc<sup>7</sup>, J. Comparat<sup>1</sup>, F. Kleinebreil<sup>2</sup>, M. Kluge<sup>1</sup>, S. Krippendorf<sup>8,9</sup>, A. Liu<sup>1</sup>, N. Malavasi<sup>1</sup>, A. Merloni<sup>1</sup>, H. Miyatake<sup>10,11,12</sup>, S. Miyazaki<sup>13</sup>, K. Nandra<sup>1</sup>, N. Okabe<sup>14</sup>, M. E. Ramos-Ceja<sup>1</sup>, J. S. Sanders<sup>1</sup>, T. Schrabback<sup>2</sup>, R. Seppi<sup>15</sup>, J. Weller<sup>1,4</sup>, and X. Zhang<sup>1</sup>

<sup>1</sup> Max Planck Institute for Extraterrestrial Physics, Giessenbachstrasse 1, 85748 Garching, Germany

<sup>2</sup> Universität Innsbruck, Institut für Astro- und Teilchenphysik, Technikerstr. 25/8, 6020 Innsbruck, Austria

<sup>3</sup> INAF, Osservatorio di Astrofisica e Scienza dello Spazio, via Piero Gobetti 93/3, I-40129 Bologna, Italy

<sup>4</sup> Department of Physics and Astronomy, Stony Brook University, Stony Brook, NY 11794, USA

<sup>5</sup> Universität Hamburg, Hamburger Sternwarte, Gojenbergsweg 112, 21029 Hamburg, Germany

<sup>6</sup> Department of Physics, National Cheng Kung University, 70101 Tainan, Taiwan

<sup>7</sup> IRAP, Université de Toulouse, CNRS, UPS, CNES, F-31028 Toulouse, France

<sup>8</sup> Universitäts-Sternwarte, Faculty of Physics, LMU Munich, Scheinerstr. 1, 81679 München, Germany

<sup>9</sup> Arnold Sommerfeld Center for Theoretical Physics, LMU Munich, Theresienstr. 37, 80333 München, Germany

<sup>10</sup> Kobayashi-Maskawa Institute for the Origin of Particles and the Universe (KMI), Nagoya University, Nagoya, 464-8602, Japan

<sup>11</sup> Institute for Advanced Research, Nagoya University, Nagoya 464-8601, Japan

<sup>12</sup> Kavli Institute for the Physics and Mathematics of the Universe (WPI), The University of Tokyo Institutes for Advanced Study (UTIAS), The University of Tokyo, Chiba 277-8583, Japan

<sup>13</sup> Subaru Telescope, National Astronomical Observatory of Japan, 650 N Aohoku Place Hilo HI 96720 USA

<sup>14</sup> Department of Physical Science, Hiroshima University, 1-3-1 Kagamiyama, Higashi-Hiroshima, Hiroshima 739-8526, Japan

<sup>15</sup> Department of Astronomy, University of Geneva, Ch. d'Ecogia 16, CH-1290 Versoix, Switzerland

February 6, 2025

### ABSTRACT

Ultra-light axions are hypothetical scalar particles that influence the evolution of large-scale structures of the Universe. Depending on their mass, they can potentially be part of the dark matter component of the Universe, as candidates commonly referred to as fuzzy dark matter. While strong constraints have been established for pure fuzzy dark matter models, the more general scenario where ultra-light axions constitute only a fraction of the dark matter has been limited to a few observational probes. In this work, we use the galaxy cluster number counts obtained from the first All-Sky Survey (eRASS1) of the SRG/eROSITA mission together with gravitational weak lensing data from the Dark Energy Survey, the Kilo-Degree Survey, and the Hyper Suprime-Cam, to constrain the fraction of ultra-light axions in the mass range  $10^{-32}$  eV to  $10^{-24}$  eV. We put upper bounds on the ultra-light axion relic density  $\Omega_a$  in independent logarithmic axion mass bins by performing a full cosmological parameter inference. We find an exclusion region in the intermediate ultra-light axion mass regime with the tightest bounds reported so far in the mass bins around  $m_a = 10^{-27}$  eV with  $\Omega_a < 0.0036$  and  $m_a = 10^{-26}$  eV with  $\Omega_a < 0.0084$ , both at 95% confidence level. When combining with CMB probes, these bounds are tightened to  $\Omega_a < 0.0030$  in the  $m_a = 10^{-27}$  eV mass bin and  $\Omega_a < 0.0058$  in the  $m_a = 10^{-26}$  eV mass bin, both at 95% confidence level. This is the first time that constraints on ultra-light axions have been obtained using the growth of structure measured by galaxy cluster number counts. These results pave the way for large surveys, which can be utilized to obtain tight constraints on the mass and relic density of ultra-light axions with better theoretical modeling of the abundance of halos.

**Key words.** galaxies: clusters: general – galaxies: clusters: intracluster medium – (cosmology:) cosmological parameters – cosmology: observations – (cosmology:) dark matter – (cosmology:) large-scale structure of Universe

## 1. Introduction

According to the Lambda Cold Dark Matter ( $\Lambda$ CDM) paradigm the Universe is composed of two species of matter: baryonic matter and cold dark matter. The latter's potential interactions with the fundamental constituents of the standard model of particle physics are below the sensitivity of modern experiments, particularly its couplings with photons. Additionally,  $\Lambda$ CDM includes a dark energy component responsible for the accelerated expansion of the Universe, which is parameterized by the cos-

mological constant  $\Lambda$ . Various cosmological probes have provided tight constraints on the dark matter, baryonic matter and dark energy content of the Universe, e.g., through the analysis of the Cosmic Microwave Background (CMB) (Planck Collaboration et al. 2016b, 2020; Hinshaw et al. 2013), Type Ia supernovae (Abbott et al. 2019; DES Collaboration et al. 2024; Scolnic et al. 2022; Brout et al. 2022), cluster abundance (Ghirardini et al. 2024, G24 hereafter, Bocquet et al. 2024, Costanzi et al. 2021, Lesci et al. 2022), weak lensing shear (Asgari et al. 2021; Abbott et al. 2022; Amon et al. 2022; Miyatake et al. 2023; Dalal

et al. 2023), and galaxy clustering (Zhao et al. 2022; DESI Collaboration et al. 2024).

Despite the constraints on the density of dark energy and dark matter obtained by state-of-the-art cosmological studies, their nature remains elusive. Consequently, potential extensions of  $\Lambda$ CDM with viable dark matter candidates have been explored using observations of the large-scale structure, e.g., axion-like particles, and self-interacting dark matter (Randall et al. 2008; Conlon et al. 2017). Axion-like particles (ALPs hereafter) are promising potential dark matter candidates. Depending on their properties, ALPs can also partially explain dark energy. ALPs are scalar fields with typically tiny masses compared to known elementary particles that move in a periodic potential. Historically, the so-called quantum chromodynamics (QCD) axion was proposed by Peccei & Quinn (1977a,b) to solve a fine-tuning problem of QCD, known as the strong charge parity (CP) problem. Although predicted by QCD, the strong CP problem refers to unobserved violations of simultaneous charge conjugation (C) and parity (P). Particles with the same underlying physics naturally occur in string theory due to the compactification of large extra-dimensions and are called axions or axion-like particles (Svrcek & Witten 2006). The typical particle masses can span the range from  $10^{-33}$  eV to  $10^{-5}$  eV. In principle, multiple ALPs with a large spectrum of mass might exist in string theory, called axiverse (Arvanitaki et al. 2010a). Upper bounds on the number of ALP species have been found by superradiance effects of stellar and supermassive black holes (Stott & Marsh 2018) and supernovae (Gendler et al. 2024). ALPs with masses  $m_a \sim 10^{-22}$  eV are dark matter candidates, while ALPs with masses  $m_a \lesssim 10^{-33}$  eV represent candidates for dark energy.

In the dark energy scenario ( $m_a \sim 10^{-33}$  eV), the axion field exhibits a slow-roll behavior due to the small mass of ALPs. As it is still rolling today, the axion field has not yet started oscillating around the minimum of its potential. Thus, it behaves like a fluid with negative pressure, similar to dark energy (Hložek et al. 2015, 2018; Passaglia & Hu 2022). For masses  $m_a \lesssim 10^{-33}$  eV, the axion field is frozen in, and only its potential energy contributes to the vacuum energy of the Universe. This scenario is indistinguishable from the  $\Lambda$ CDM dark energy with the equation of state  $w = -1$ .

In the case of small masses around  $10^{-24}$  eV, the bosonic nature and negligible self-couplings of ALPs enable them to form the Bose-Einstein condensates (BECs) on scales determined by their thermal de-Broglie wavelength. In this axion mass regime, the thermal de-Broglie wavelength extends to the cosmological scales, i.e., several kilo- or megaparsec, making the axion condensates observable in studies of the matter power spectrum. A BEC on these scales forms large core-like structures, smoothes out the dark matter distribution, and suppresses the formation of small-scale halos, potentially solving the small-scale crisis of cosmology (Nori & Baldi 2018). We refer to these cosmologically interesting low-mass axions with masses  $m_a \lesssim 10^{-24}$  eV as ultra-light axions (ULAs) hereafter. In the literature, the resulting dark matter is also referred to as fuzzy dark matter (FDM) due to its smoothing effect (e.g. Hu et al. 2000; Hui et al. 2017).

At higher axion mass scales ( $m_a \gtrsim 10^{-22}$  eV), it is possible to constrain the coupling constant between ALPs and photons. This requires direct X-ray measurements of the intra-cluster medium (ICM), which have the potential to detect a possible interaction between axions and photons. Such an interaction is only possible in magnetic fields since the axion coupling term is proportional to the scalar product of electric and magnetic fields. Measurements of spectral features in galaxy clusters have been used to constrain the properties of dark matter candidates such

as ALPs and decaying dark matter (Bulbul et al. 2014; Conlon et al. 2017; Reynolds et al. 2020). Unlike the studies performed with the probes of structure growth, these analyses can determine bounds on the axion-photon coupling constant and mixing angles, but they cannot constrain the relic density of dark matter candidates.

The viable mass ranges for ULAs and abundances constituting dark matter and dark energy can be constrained through observations of the large-scale structure as well as the cosmic microwave background and sub-galactic scales. In the dark matter regime, where the ULAs make up all of dark matter by assumption, strong bounds on the ULA parameter space have been reported in the literature. Lyman-alpha forest observations place a lower mass bound of  $2 \times 10^{-20}$  eV (Rogers & Peiris 2021), while superradiance by supermassive black holes sets a lower bound in mass of  $7 \times 10^{-20}$  eV (Stott & Marsh 2018), both at 95% confidence level. The observations of ultra-faint dwarf galaxies tighten this bound to  $3 \times 10^{-19}$  eV at 99% confidence level (Dalal & Kravtsov 2022).

However, the possibility that ULAs may comprise only a fraction of the total abundance of dark matter remains. CMB data from the Planck satellite (Planck Collaboration et al. 2016a) provided for the first time strong bounds in the mass regime  $10^{-32}$  eV to  $10^{-25}$  eV by performing a binned analysis in different ULA mass bins. They find varying upper bounds on the ULA abundance, reaching down to  $\Omega_a \lesssim 0.01$  in the intermediate mass range between  $10^{-30}$  –  $10^{-27}$  eV (Hložek et al. 2015, 2018). The same mass regime has also been constrained by Laguë et al. (2022) and Rogers et al. (2023) using Planck 2018 (Planck Collaboration et al. 2020) and Baryon Oscillation Spectroscopic Survey (BOSS) (Alam et al. 2017) data, improving existing constraints. Kobayashi et al. (2017) used the Lyman- $\alpha$  forest to place bounds on the fraction of ULAs in the higher mass regime  $10^{-23}$  eV to  $10^{-20}$  eV and Winch et al. (2024) closed the gap by using UV-bright galaxy abundance to put an upper bound on the ULA fraction in the mass regime  $10^{-26}$  eV to  $10^{-23}$  eV. They find that ULAs cannot make up more than 22% of all dark matter in this mass range.

In this work, we use for the first time the observed abundance of galaxy clusters to constrain the parameter space of ULAs. Since the formation of halos is influenced by bosonic condensation, we expect cluster counts to be sensitive to ULAs (Diehl & Weller 2021). We particularly focus on the mass regime  $10^{-32}$  eV to  $10^{-24}$  eV. Clusters of galaxies trace the highest peaks in the low-redshift matter density field through their number counts and, therefore, serve as an important late-time probe of the structure formation in the Universe. Measurements of their number count as a function of mass, and redshift bin per unit volume, the so-called cluster halo mass function (HMF), is a sensitive probe of cosmology. The cluster mass function can constrain the ULA mass and abundance parameter space since the growth of structure and bosonic condensation influence the formation of halos.

To this end, we use the clusters of galaxies detected by the extended ROentgen Survey with an Imaging Telescope Array (eROSITA) on board the Spektr-RG (SRG) mission (Sunyaev et al. 2021) during its first All-Sky Survey in the Western Galactic Hemisphere (eRASS1). eROSITA, launched in 2019, scans the sky in the soft X-ray band with its highest sensitivity in the 0.2 to 2.3 keV energy band (Predehl et al. 2021). eRASS1 provides different cluster catalogs depending on purity and completeness requirements. The primary eRASS1 catalog comprises 12,247 galaxy clusters, with a sample purity of 86% and a coverage of  $12,791 \text{ deg}^2$  (Bulbul et al. 2024; Kluge et al. 2024). In

this work, we use the cosmology sample, containing 5,259 securely detected clusters in the redshift range of  $0.1 \leq z \leq 0.8$  having a sample purity of 96%. The eRASS1 cosmological sample provided competitive results for standard cosmologies (see G24 for the details of the analysis), as well as modified gravity (Artis et al. 2024b), and the growth of structures (Artis et al. 2024a, subm. to A&A). The eRASS1 cosmology sample is the largest ICM-selected galaxy cluster sample ever used to infer cosmology from number counts. The covered cluster mass range extends down into the galaxy group regime, opening the possibility of probing cosmological models sensitive to below-cluster scales. The presence of ULAs has the strongest imprint on the number density of low-mass halos, making the eRASS1 cosmology sample a promising tool to constrain the properties of ULAs. In contrast to the main cosmological inference G24, in this work, to constrain the ULA parameter space, we use the Boltzmann solver axionCAMB instead of CAMB to compute a matter power spectrum that is sensitive to two ULA parameters, particularly the mass of the ULA  $m_a$  and the energy density fraction of ULAs  $\Omega_a$  in units of the critical density of the Universe.

This paper is organized as follows. A more detailed overview of ULAs and their effect on cosmology is given in Sect. 2, including their influence on structure formation. The underlying cosmological sample of the eRASS1 survey and the optical and weak lensing data used for the analysis are summarized in Sect. 3. Section 4 reviews the eRASS1 cluster cosmological pipeline for Bayesian inference in light of ULA parameters. The results are presented and discussed in Sects. 5 and 6. For better readability, we use natural units  $c \equiv \hbar \equiv 1$  throughout this work.

## 2. Ultra-light Axion Cosmology

In this section, we first provide a review of the motivation for ULAs as dark matter candidates and the implications of their existence on the hierarchical structure formation and cosmology.

### 2.1. Physical Origin of Axions

Axions are hypothetical pseudoscalar particles with typically low mass (between  $10^{-33}$  eV and  $10^{-5}$  eV) and weak couplings to the Standard Model particles (i.e., quadratic coupling terms can be neglected). Pseudoscalar hereby refers to the property that the particle behaves like a scalar under transformations, except parity transformations, under which it switches signs. Although the axion was originally introduced in QCD to solve the strong CP problem explicitly, the term has been extended to a number of (pseudo) Nambu-Goldstone bosons. Nambu-Goldstone bosons are particles that occur as massless degrees of freedom after breaking a spontaneous symmetry. Axions are pseudo-Nambu-Goldstone bosons as they acquire a very small mass via further symmetry breaking. These particles appear in various quantum field theories such as string theory (e.g. Svrcek & Witten 2006; Conlon 2006; Arvanitaki et al. 2010b) or supersymmetric extensions of the Standard Model (e.g. Kim & Carosi 2010; Marsh 2016, for review). To distinguish such general axions from the QCD axion, they are often referred to as axion-like particles or ultra-light axions in the cosmologically relevant low mass regime. The common properties of these particles are well described in section 2.2 in Marsh (2016).

We heuristically illustrate axion physics using the QCD axion introduced by Peccei & Quinn (1977a,b) as a generic example. We refer the reader to Marsh (2016) for further details. A non-Abelian SU(3) gauge theory with a gluon gauge field  $G_{\mu\nu}^a$

naturally exhibits a topological term with some coupling  $\theta$  in its Lagrangian density, which is of the form:

$$\mathcal{L} \supset \frac{\theta}{32\pi^2} G_{\mu\nu}^a \tilde{G}^{a\mu\nu}, \quad (1)$$

where  $\tilde{G}^{a\mu\nu} = \epsilon^{\mu\nu\alpha\beta} G_{\alpha\beta}^a / 2$  is the dual of the gluon gauge field tensor,  $\mu$  and  $\nu$  refer to spacetime coordinates and  $a$  is some color index. This term is CP-violating and cannot be transformed away. If QCD is CP-violating, it leads to a non-vanishing neutron electric dipole moment  $d_n \approx \theta (3.6 \times 10^{-16} e \text{ cm})$  (Crewther et al. 1979). However, experiments place strong constraints on the neutron electric dipole moment (Abel et al. 2020), which results in a fine-tuned value of  $\theta \lesssim 10^{-10}$ . In other words, QCD appears to be non-CP-violating, although it should. This is known as "the strong CP problem".

Peccei & Quinn (1977a,b) solved this problem by generalizing the coupling constant  $\theta$  to a scalar field that naturally cancels any contribution to the CP-violating term. To this end, they introduced a new global  $U_{PQ}(1)$  symmetry, known as the *Peccei-Quinn symmetry*. The spontaneous breaking of this symmetry at a high energy scale  $f_a$  leads to a vacuum manifold that is isomorphic to the one-sphere  $S^1$ . The emerging Nambu-Goldstone boson (which will become the axion later) is an angular degree of freedom in an effectively flat potential. Thus, at this point, the new particle is massless. At some lower energy scale,  $\Lambda_a$  (not to be confused with the cosmological constant  $\Lambda$ ), non-perturbative QCD effects (e.g., instantons, topological effects) break the flatness of the vacuum manifold, the massless Nambu-Goldstone boson lives in. Due to the angular nature of the Nambu-Goldstone boson, only a discrete angular shift symmetry is preserved. Ultimately, the Nambu-Goldstone boson acquires a mass and is canonically called an axion. Simplifying further, the field rolls into the circular minimum of a Mexican-hat-like potential during the first spontaneous symmetry breaking. The Nambu-Goldstone boson is the angular degree of freedom that moves freely along the minimum of the potential. The angular shift symmetry of this potential is then broken by non-perturbative effects, leading to local minima and maxima along the former circular minimum of the potential. Particles moving in a potential with minima acquire a mass; thus, the Nambu-Goldstone boson becomes a massive axion particle.

The axion mass is related to the symmetry-breaking scales  $f_a$  and  $\Lambda_a$ . A typical but not unique effective axion potential can take the form:

$$V(\phi) = \Lambda_a^4 \left[ 1 - \cos\left(\frac{\phi}{f_a}\right) \right]. \quad (2)$$

Considering small oscillations around one of the local minima gives the effective mass of the axion by approximating the local environment of the minimum with a quadratic function:

$$V(\phi \approx \phi_{\min}) \approx \frac{1}{2} \left( \frac{\Lambda_a^2}{f_a} \right)^2 \phi^2 + \Lambda_a^4 \mathcal{O}\left(\frac{\phi^4}{f_a^4}\right) \quad (3)$$

$$= \frac{1}{2} m_a^2 \phi^2 + (\text{self-interactions}). \quad (4)$$

The mass of the axion can be read off as  $m_a = \Lambda_a^2 / f_a$ . Self-interactions are negligible in all relevant mass regimes (especially for the ultra-light mass regime) since the quartic coupling constant is smaller than the square of the axion mass  $m_a^2$

by a factor of  $1/f_a^2$ . Typical values of  $f_a$  lie between  $10^9$  GeV and  $10^{17}$  GeV in the QCD case and, in the general case, above  $10^{10}$  GeV with typical values around the grand unified theory (GUT) scale at  $10^{16}$  GeV (Marsh 2016). In all cases, self-interactions are heavily suppressed and can safely be considered negligible in our analysis.

The underlying mechanisms of the QCD axion also apply to axions in string theory models. However, in string theory, the periodicity of the axion potential originates from the compactification of extra dimensions, i.e., extra dimensions are wrapped up, which makes them unobservable by macroscopic observers. The need for extra dimensions in string theory, which have not been observed yet, leads to a natural production mechanism of axion particles with a potentially wide range of possible axion masses.

## 2.2. Cosmological Implications of Ultra-light Axions

This section reviews the implications of an ultra-light axion fluid on cosmology. For in-depth discussion and derivations, we refer the reader to the derivations presented in Marsh (2016), Hložek et al. (2015), and Hložek et al. (2018). The ULA field enters the Einstein-Hilbert action of general relativity as a massive scalar field in curved spacetime. On a Friedmann-Lemaître-Robertson-Walker metric background, the Klein-Gordon equation (equation of motion) of the ULA is:

$$\ddot{\phi} + 3H\dot{\phi} + m_a^2\phi^2 = 0. \quad (5)$$

Here,  $H(t) = \dot{a}(t)/a(t)$  is the Hubble parameter,  $\phi$  is the ULA field, and dots refer to derivatives in time. This equation describes a harmonic oscillator in  $\phi$  with a damping term proportional to Hubble parameter  $H$ . For this illustration, we neglect any source terms from other cosmological fluid components or self-interactions, which would enter the equation on the right-hand side and replace the zero. For  $H \ll m_a$ , i.e., if the ULA mass is orders of magnitude larger than the Hubble parameter, the damping term is negligible, and the ULA field oscillates freely. If the ULA's mass is sufficiently large, this describes the matter-like late-time behavior of the ULA. For the opposite case,  $H \gg m_a$ , the field is overdamped and frozen in, showing the same behavior as dark energy. The transition between the two regimes defines a scale  $a_{\text{osc}}$  which can be approximated by  $H(a_{\text{osc}}) \approx m_a$ . In this regime, the ULA is slow-rolling. Thus, a single ULA species may transition from a dark energy-like behavior to a dark matter-like behavior. As the Universe evolves in the opposite direction from matter-dominated to dark energy-dominated era, no single ULA species can describe both dark matter and dark energy. We therefore distinguish two distinct phenomenological regimes for ULAs: the dark matter regime, where they behave as dark matter, and the dark energy regime, where they show the same observed effect of dark energy. We review the two regimes in the following subsections.

## 2.3. Dark Matter Regime of Ultra-light Axions

Introducing perturbations to the ULA field and choosing a gauge yields an equation for the evolution of perturbations in terms of the ULA overdensity  $\delta_a = \delta\rho_a/\rho_a$ . In the simple case of an ULA-dominated Universe, it takes the form:

$$\ddot{\delta}_a + 2H\dot{\delta}_a + \left( \frac{k^2 c_{s,a}^2}{a^2} - 4\pi G\rho_a \right) \delta_a = 0, \quad (6)$$

where  $k$  is the wave number,  $a$  the scale factor,  $\rho_a$  describes the background density field of the ULA,  $\delta\rho_a$  its perturbation. Other potential fluid components would add source terms to the equation. The effective sound speed of ULAs ( $c_{s,a}$ ) becomes

$$c_{s,a}^2 = \frac{k^2}{k^2 + 4m_a^2 a^2}. \quad (7)$$

Equation 6 defines a scale-dependent Jeans scale  $k_J$  for ULAs. As described in Marsh (2016), large-scale perturbations ( $k < k_J$ ) grow and behave similarly to CDM. Small-scale perturbations ( $k > k_J$ ) oscillate, making them distinct from CDM perturbations on the same scales. As described in Marsh et al. (2012), modes entering the horizon while the ULA sound speed in Eq. 7 is near the speed of light will suppress structure formation while modes entering the horizon while the ULA sound speed is approaching zero will cluster like ordinary cold dark matter. Effectively, this translates to suppressing the matter power spectrum on small physical scales (large values of the wave number  $k$ ).

The properties of ULAs and their cosmological effects can be described with two quantities: The particle mass of the ULA  $m_a$ , and the relative energy density of ULAs with respect to the critical density of Universe,  $\Omega_{\text{ax}} = \rho_{\text{ax}}/\rho_{\text{crit}}$ , also known as the relic density of ULAs. Here, the critical density of the Universe is defined as  $\rho_{\text{crit}} = 3H_0^2/(8\pi G)$ . The  $\Lambda$ CDM cosmology is recovered when  $\Omega_a \rightarrow 0$ . Furthermore, the ULAs' suppression imprint on the matter power spectrum becomes negligible for high ULA masses  $m_a \gg 10^{-22}$  eV, effectively recovering a  $\Lambda$ CDM cosmology in the context of this analysis. Figure 1 demonstrates the suppression effect of ULA dark matter with different logarithmic particle masses  $\log_{10}(m_a[\text{eV}])$  and relic densities  $\Omega_a$  on the matter power spectrum. Suppression of the power can be seen on small scales (large  $k$ ), whereby the effect is stronger with higher ULA fractions or lower ULA masses.

In this work, we explore if a fraction of dark matter is composed of ULAs of an unknown mass in the dark matter regime. We still need to postulate a cosmological constant dark energy in this context. As we assume a flat Universe, the dark energy density is given by  $\Omega_\Lambda = 1 - \Omega_m - \Omega_a$ , while we fit for the total matter density  $\Omega_m$  and the ULA density  $\Omega_a$ . The results are provided in Sect. 5.

### 2.3.1. Dark Energy Regime of Ultra-light Axions

If the ULA is so light that its mass becomes comparable with or smaller than the Hubble parameter  $H_0$ , the oscillation scale  $a_{\text{osc}}$  approaches or even exceeds the current scale factor of the Universe  $a(z=0) = 1$ , indicating that the ULA field did not start oscillating yet. Indeed, this kind of field behaves as dark-energy-like, which can be heuristically illustrated with the equation of motion. Neglecting the  $m_a^2\phi^2$  term in Eq. 5 and assuming that  $H(t)$  varies slowly enough in time exhibits exponential modes for the ULA field  $\phi$ . This behavior is associated with an equation of state  $w_{\text{ax}} \approx -1$  via the density and pressure of the ULA field. This leads to a redshift-dependent equation of state whose transition from a dark matter to a dark energy behavior depends on the ULA mass. Figure 2 illustrates the dependence of the oscillation redshift on the ULA mass. At the oscillation redshift, the ULA field starts to oscillate in the minimum of its potential well and thus exhibits particle-like (dark matter-like) behavior.

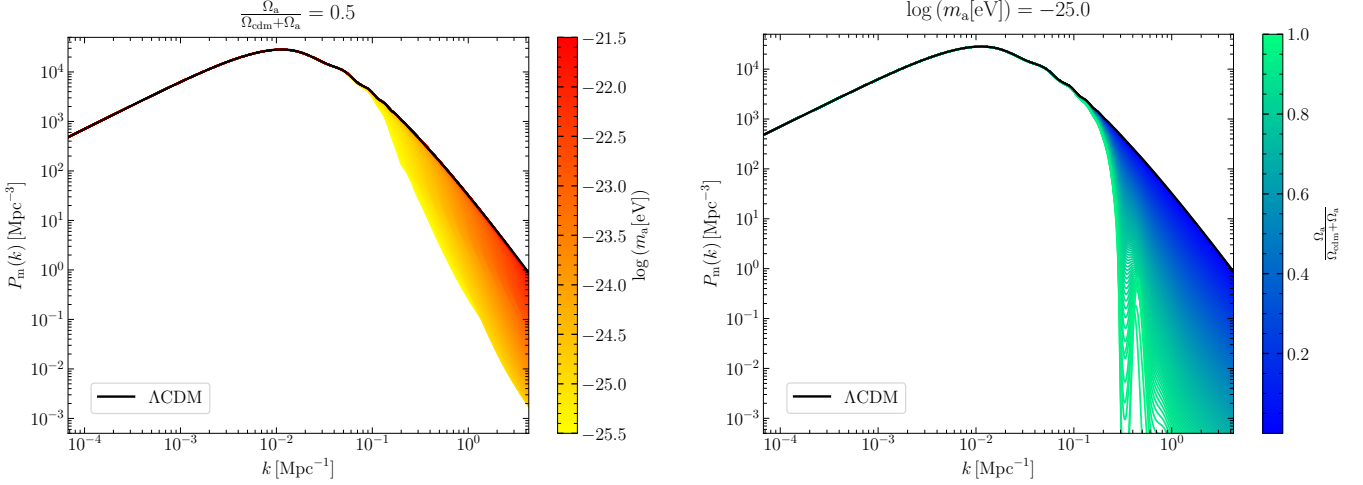


Fig. 1: The effect of ULAs on the matter power spectrum recovered assuming the [Planck Collaboration et al. \(2020\)](#) cosmological values ( $\Omega_\Lambda \approx 0.7$ ,  $\Omega_m + \Omega_a \approx 0.3$ ) at  $z = 0.1$  is shown. On the left, the change in the matter power spectrum with varying ULA mass is shown when the relative ULA density is fixed to  $\Omega_a/(\Omega_{\text{cdm}} + \Omega_a) = 0.5$ . The figure on the right displays the dependence of the power spectrum on varying ULA abundance at a fixed ULA mass of  $m_a = 10^{-25}$  eV. The concordance  $\Lambda$ CDM model is shown in a black curve on both panels. Small-scale suppression becomes stronger with decreasing ULA mass and increasing ULA abundance. For higher ULA masses of  $m_a \gg 10^{-22}$  eV, the matter power spectrum becomes indistinguishable from the one in a  $\Lambda$ CDM cosmology, as is the case for  $\Omega_a \rightarrow 0$ .

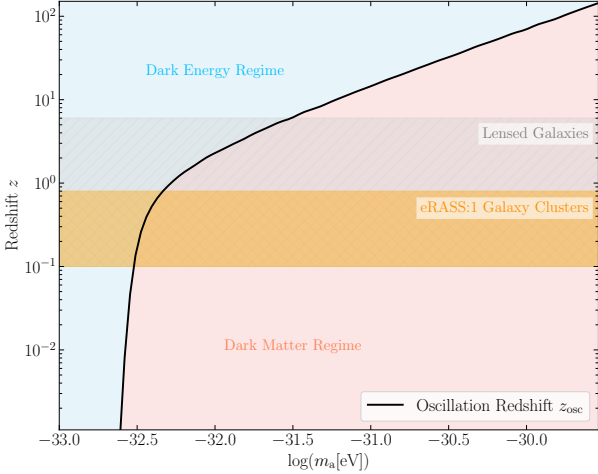


Fig. 2: Demonstration of the ULA mass and redshift dependent regime change. The orange shaded region shows the eRASS1 cluster redshift range, the gray shaded region shows the redshift range of lensed galaxies from the DES, HSC and KiDS data, described in Sect. 3.2. Above a ULA mass of  $m_a \sim 10^{-31.5}$  eV, the regime change does not affect the distance measurements during the parameter inference. For ULAs with a masses below  $m_a \sim 10^{-31.5}$  eV the distance measurements are affected by the regime change via the Hubble rate. This exclusively impacts the lowest ULA mass bin, which has been appropriately accounted for.

### 3. Multi-wavelength data

#### 3.1. eROSITA Cluster Catalog and X-ray Observable

This work uses the cosmology sample compiled from the first eROSITA All-Sky Survey ([Merloni et al. 2024](#); [Bulbul et al. 2024](#); [Kluge et al. 2024](#)). This sample is constructed by employing an extent likelihood cut of  $\mathcal{L}_{\text{ext}} > 6$  and a redshift range of  $0.1 \leq z \leq 0.8$ . The publicly available DESI Legacy Survey Data Release 10 data (LS DR10) is used for the confirmation, identification, and photometric redshift measurements of the X-ray-selected cluster candidates detected in the eROSITA All-Sky Survey’s Western Galactic Hemisphere ([Kluge et al. 2024](#)). The common footprint between eRASS1 and the LS DR10-South footprint is  $12,791 \text{ deg}^2$ , and contains 5,259 securely confirmed clusters ([Kluge et al. 2024](#)). Its purity level is estimated to be 96%.

The eROSITA X-ray data is reprocessed with the eSASS software as described in [Merloni et al. \(2024\)](#) by applying a correction for the Galactic absorption and a more accurate ICM and background modeling. The details of the X-ray processing are provided in [Bulbul et al. \(2024\)](#); [Liu et al. \(2022\)](#). The X-ray observable count rate in the observer frame, which demonstrates a tight correlation with weak lensing shear data and is related to selection, is used as a mass proxy for this work, similar to the method adopted in [G24](#).

#### 3.2. Weak Lensing Data

In order to minimize the bias on galaxy cluster masses, we use weak gravitational lensing data to obtain reliable mass measurements for the calibration of the mass-observable scaling relations.

We use weak lensing measurements in the form of tangential reduced shear profiles extracted from the shapes of background galaxies in the Dark Energy Survey year three (DES Y3) data ([Sevilla-Noarbe et al. 2021](#); [Gatti et al. 2021](#)) and the Kilo De-

gree Survey (KiDS), and Hyper Suprime-Cam (HSC) Strategic Survey program (Hildebrandt et al. 2021; Li et al. 2022). The details of shape measurements around the detected eROSITA clusters and the weak lensing mass calibration details are provided in Grandis et al. (2024) and Kleinebreil et al. (2024). Besides the reduced tangential shear profile, we also use estimates of the redshift distribution for the employed background sources, estimates of the measurement uncertainty on the reduced shear profile, and calibrations on the contamination of the background sample by cluster member galaxies.

DES shares a common sky area of  $4,060 \text{ deg}^2$  with eROSITA and has conducted observations in the  $r$ ,  $i$ , and  $z$  bands (Sevilla-Noarbe et al. 2021). The details of the application of the DES Y3 shear maps to the eRASS1 galaxy clusters are presented in Grandis et al. (2024). Tangential shear profiles were derived from the DES Y3 shape catalog (Gatti et al. 2021). The analysis yields 2,201 tangential shear profiles for eRASS1 galaxy clusters with a signal-to-noise ratio of 65.

The Hyper Suprime-Cam (HSC) Subaru Strategic Program (Aihara et al. 2018) is a wide and deep optical survey in the  $g$ ,  $r$ ,  $i$ ,  $z$ , and  $y$  bands. The three-year shape catalog (HSC Y3) (Li et al. 2022) was used to analyze galaxy cluster shear profiles in an overlapping sky area of  $\approx 500 \text{ deg}^2$  between HSC Y3 and eRASS1. This analysis yielded tangential shear profiles, lensing covariance matrices, and redshift distributions for 96 eRASS1 galaxy clusters. The total signal-to-noise is 40.

The Kilo-Degree Survey (KiDS) is an optical wide-field survey in the  $u$ ,  $g$ ,  $r$ , and  $i$  bands, dedicated to delivering weak gravitational lensing as well as photometric redshift measurements (de Jong et al. 2013). We use the shear maps and photometric redshifts of the fourth data release of the Kilo-Degree Survey (KiDS-1000) over a sky area of  $\approx 1,000 \text{ deg}^2$  (Kuijken et al. 2019; Giblin et al. 2021; Hildebrandt et al. 2021; Wright et al. 2020). The joint sky coverage with eROSITA yielded reduced tangential shear maps for 237 eRASS1 galaxy clusters (101 in the KiDS-North field, 136 in the KiDS-South field) with a total signal-to-noise of 19 (for details see Kleinebreil et al. 2024).

We highlight the importance of the overlap between eRASS1 clusters in KiDS and HSC (125 clusters) and in KiDS and DES (25 clusters). There is no overlap in the sky coverage of HSC and DES, so the reduced tangential shear maps deduced from KiDS-1000 provide an internal consistency check (Kleinebreil et al. 2024, G24).

## 4. Methodology

This section briefly presents the inference pipeline developed in G24 and explains the applied adaptations to consider the cosmological effects of introducing ultra-light axions. To this end, we review the observables, the HMF, the mass-observable scaling relations, and the weak gravitational lensing calibration.

The forward modeling cosmological pipeline is described in G24. It takes into account selection effects through the selection function presented in Clerc et al. (2024) to model the completeness and mass-observable scaling laws calibrated with weak gravitational lensing data by DES Y3, KiDS, and HSC Y3, presented in Grandis et al. (2024); Kleinebreil et al. (2024), as well as a mixture model for eliminating care of possible contaminants (Kluge et al. 2024). The Bayesian analysis assumes a Poissonian likelihood for the galaxy cluster number counts. The pipeline is used for constraining a large set of cosmological parameters as well as scaling parameters simultaneously.

### 4.1. Statistical inference

This section summarizes the framework presented in G24 for the computation of the cluster count likelihood. The cluster abundance  $n$  per units of true mass  $M$ , true redshift  $z$ , and solid angle (true sky positions are noted  $\mathcal{H}$ ) follows

$$\frac{dn}{d \ln M d z d \mathcal{H}} = \frac{\rho_{m,0}}{M} \frac{d \ln \sigma^{-1}}{d \ln M} f(\sigma) \frac{d V}{d z d \mathcal{H}}, \quad (8)$$

where  $\rho_{m,0}$  is the matter density at present,  $\sigma(R, z)$  is the root mean square density fluctuation defined below,  $d V/d z d \mathcal{H}$  is the differential comoving volume per redshift per steradian.  $f(\sigma)$  is the multiplicity function introduced by Tinker et al. (2008), with its parameters assumed to be fixed and universal. The root mean square density fluctuation  $\sigma$  is defined as the variance of a convolution of the square of a window function  $W$  with the matter power spectrum  $P$ :

$$\sigma^2(z, R) = \int_0^\infty dk k^2 P(k, z) |W(kR)|^2, \quad (9)$$

where  $k$  is the wave number of the considered mode, and  $R$  is the defining radius of the corresponding overdensity. For  $W$ , the standard top-hat window function is used, defined as the Fourier transform of a radially symmetrical uniform density distribution up to a certain radius;

$$W(kR) = \int_{\mathbb{R}^3} d^3 \mathbf{r} \frac{3\Theta(R-r)}{4\pi R^3} e^{-i\mathbf{k}\mathbf{r}} = 3 \frac{\sin(kR) - (kR) \cos(kR)}{(kR)^3}. \quad (10)$$

The observed cluster number density is assumed to follow a Poisson statistic, as commonly performed in modern cluster surveys (e.g. Bocquet et al. 2024). We do not consider the sample variance (Hu & Kravtsov 2003), as its impact is negligible given the characteristics of the eRASS1 survey (i.e., a catalog of massive halos and a large volume, see Fumagalli et al. 2021). We note as  $\lambda$  the intensity of the Poisson process (the number density of objects per unit of observable) and  $x$  as the vector of the observables. This intensity depends on the background cosmological model. We note as  $\Theta$  the set of cosmological parameters used. By definition, the expected number of objects whose observable properties belong to the sub-sample  $\Omega$  of the observable parameter space follows;

$$N_{\{x \in \Omega\}}(\Theta) = \int_{\Omega} \lambda(x|\Theta) dx. \quad (11)$$

In the case of eRASS1, combined with the observation of the Legacy Survey DR10 (Kluge et al. 2024), the observable vector incorporates the observed X-ray count rate  $\widehat{C}_R$ , the observed optical richness  $\widehat{\lambda}$ , the photometric redshift  $\widehat{z}$ , the observed sky position  $\widehat{\mathcal{H}}$ , and the reduced tangential shear profile  $\widehat{g}_t$  for clusters that belong to the overlapping weak lensing surveys used for the mass calibration. The vector of observables consequently reads

$$x = \{\widehat{C}_R, \widehat{z}, \widehat{\lambda}, \widehat{\mathcal{H}}, \widehat{g}_t\}.$$

We can thus rewrite the intensity of the Poisson process as  $\lambda(x|\theta) = (d\hat{n})/(\widehat{dC_R d\lambda d\hat{g}_i d\hat{z} d\mathcal{H}})$ , with

$$\frac{d\hat{n}}{\widehat{dC_R d\lambda d\hat{g}_i d\hat{z} d\mathcal{H}}} = \int \frac{dn}{d\ln M dz d\mathcal{H}} \mathcal{P}(x|M, z) \mathcal{P}(I|x) d\ln M dz, \quad (12)$$

where  $\mathcal{P}(x|M, z)$  is the probability distribution function related to the observables at a given mass and redshift (see Sect. 4.3), and  $\mathcal{P}(I|x)$  is the selection function, describing the expected fraction of objects that we detect for a given set of observable  $x$ , described in Sect. 4.2.

#### 4.2. Selection function

The selection function model  $\mathcal{P}(I|x)$  was produced using the state-of-the-art eRASS1 digital twin simulation (Seppi et al. 2022; Comparat et al. 2020). The simulation reproduces the AGN and cluster distributions with high accuracy and produces synthetic eRASS1 observations. A detection probability is assigned to each set of observables using a Gaussian process classifier described in Clerc et al. (2024). In practice, the observables used to assign the probability are the true redshift  $z$ , the galactic column density  $n_{\text{H}}$ -corrected count rate  $C_R$ , and the sky position  $\mathcal{H}$ . The selection function depends on the sky position through the local background surface brightness, the local hydrogen column density, and the exposure time, which are not uniform across the eRASS1 sky. The selection function enters the statistical inference framework as described in Sect. 4.1.

#### 4.3. Scaling relations

The eRASS1 cluster abundance pipeline primarily considers two mass proxies: the X-ray count rates  $C_R$  and the optical richness  $\lambda$ . The scaling relations between these observables and the underlying dark matter halo mass are fitted together with the cosmological parameters. The count rate scaling relation is assumed to follow

$$\left\langle \ln \frac{C_R}{C_{R,p}} \middle| M, z \right\rangle = \ln A_X + b_X(z) \ln \frac{M}{M_p} + e_X(z), \quad (13)$$

where the pivot count rate, pivot mass, and pivot redshift are fixed to  $C_{R,p} = 0.1$  cts/s,  $M_p = 2 \times 10^{14} M_\odot$ , and  $z_p = 0.35$  by choice. The other terms follow

$$b_X(z) = B_X + F_X \ln \frac{1+z}{1+z_p}, \quad (14)$$

and

$$e_X(z) = D_X \ln \frac{d_L(z)}{d_L(z_p)} + E_X \ln \frac{E(z)}{E(z_p)} + G_X \ln \frac{1+z}{1+z_p}. \quad (15)$$

The richness scaling relation has a similar form with

$$\left\langle \ln \lambda \middle| M, z \right\rangle = \ln A_\lambda + b_\lambda(z) \ln \left( \frac{M}{M_p} \right) + C_\lambda \ln \left( \frac{1+z}{1+z_p} \right), \quad (16)$$

and the redshift dependence of the mass slope follows

$$b_\lambda(z) = B_\lambda + D_\lambda \ln \left( \frac{1+z}{1+z_p} \right). \quad (17)$$

These scaling relations bridge the X-ray, optical, and shear data. They enter into the statistical inference framework via  $\mathcal{P}(x|M, z)$ , as described in Sect. 4.1.

#### 4.4. Weak Lensing Calibration

To accurately predict the mapping between halo mass and weak lensing profiles, we employ the shear inferred cluster mass, which results from fitting a reduced shear profile with our custom shear profile model, as proposed by Grandis et al. (2021). The relation between weak lensing mass and halo mass is parametrized with the weak lensing bias and weak lensing scatter. The values of the latter, as well as their uncertainties, are calibrated on the Monte-Carlo realizations of synthetic shear profiles (Grandis et al. 2024). These synthetic shear profiles are based on mass maps from hydrodynamical simulations augmented by the eRASS1 mis-centering distribution, by the cluster member contamination results, by the shape and photometric redshift calibration uncertainties of respective weak lensing surveys, and by an uncorrelated large-scale structure noise contribution. We also add a flat 2% uncertainty due to the possible suppression of cluster matter profiles in the central region caused by baryon feedback effects (Grandis et al. 2021). We make the reasonable modelling assumption that these calibrations will remain valid over the full ULA mass range for small ULA fractions  $\Omega_a/(\Omega_{\text{cdm}} + \Omega_a) \lesssim 0.1$ , since simulations do not show evidence for ULA effects on halo density profiles below this threshold (Schwabe et al. 2020; Vogt et al. 2023). As discussed below, even for a dark matter sector comprised solely by ULAs ( $\Omega_a/(\Omega_{\text{cdm}} + \Omega_a) = 1$ ) the calibrations remain valid for  $m_a \gtrsim 10^{-26}$  eV.

The presence of ULA dark matter impacts the structure of halos, as explored most completely in gravity-only simulations in May & Springel (2023). Those simulations confirm prior phenomenological findings of Schive et al. (2014); Marsh (2016) that axion-like particles form a so-called soliton core where quantum degeneracy pressure compensates for the inward pull of gravity in the inner regions of halos. The density profile of the core can be analytically approximated as

$$\rho_{\text{sol}}(r) = \frac{1.9 \times 10^9 (1+z) \left( \frac{m_a}{10^{-23} \text{ eV}} \right)^{-2} \left( \frac{r_{\text{sol}}}{\text{kpc}} \right)^{-4}}{\left( 1 + 0.091 \left( \frac{r}{r_{\text{sol}}} \right)^2 \right)^8} M_\odot \text{ kpc}^{-3}, \quad (18)$$

where  $z$  is the halo redshift. The characteristic radius of the soliton cores  $r_{\text{sol}}$  marks the scale at which the density profile transitions from a flat inner part to a steeply declining outer part. Such core profiles for different ULA particle masses  $m_a$ , and halo masses  $M$  at redshift  $z = 0.1$  are shown in the left panel of Fig. 3 as dotted lines. Crucial to the phenomenology of halo profiles in ULA cosmology is the halo mass dependence of the core radius, given by Schive et al. (2014) as

$$r_{\text{sol}} = 1.6 \left( \frac{m_a}{10^{-22} \text{ eV}} \right)^{-1} (1+z)^{1/2} \left( \frac{\zeta(z)}{\zeta(0)} \right)^{1/6} \left( \frac{M}{10^9 M_\odot} \right)^{-1/3} \text{ kpc}, \quad (19)$$

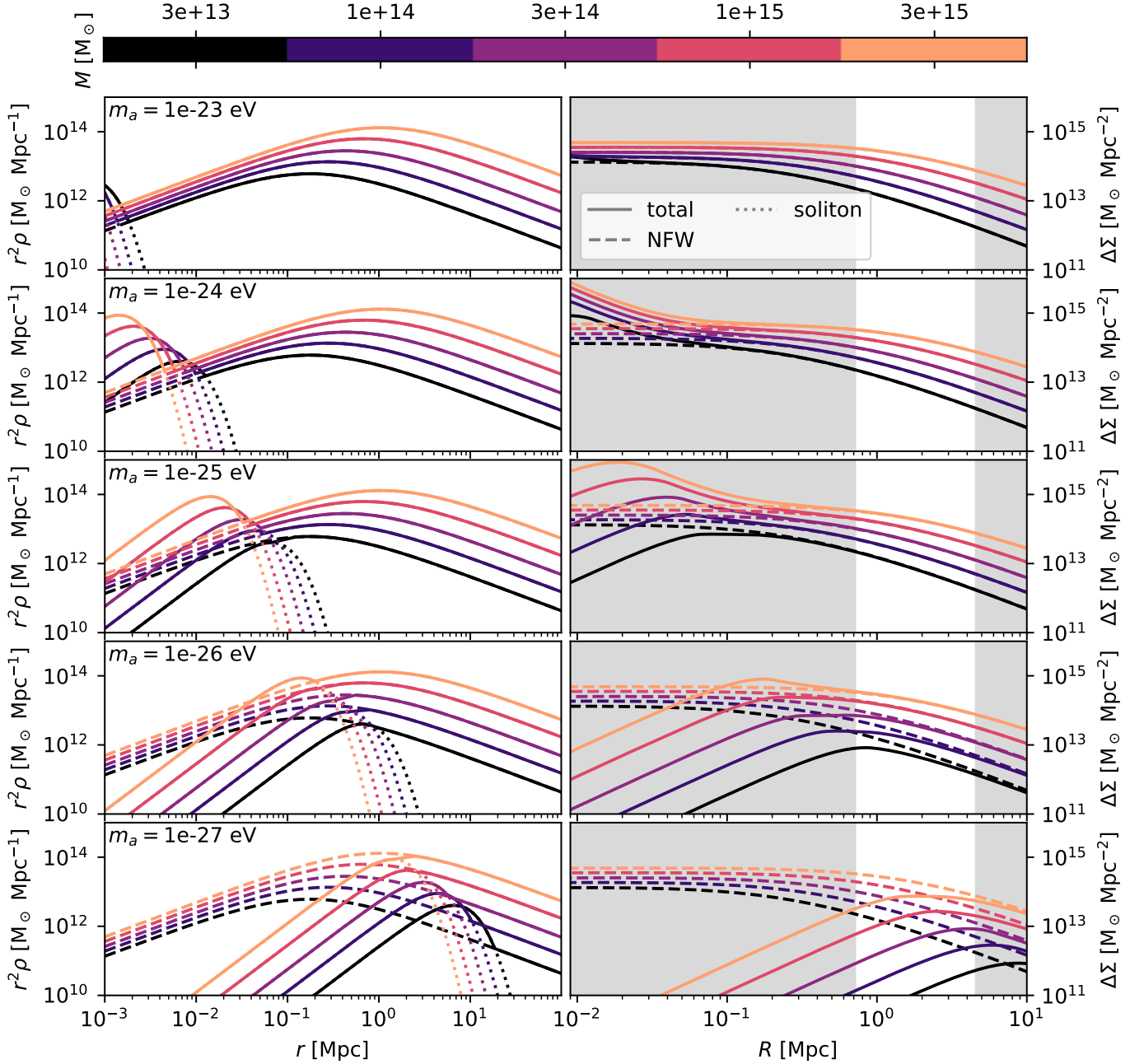


Fig. 3: Density profiles (left column) and projected density contrasts (right column) of halos of different mass (color-coded) at redshift  $z = 1$  for different ULA particle masses (rows) in the extreme case of a ULA-only dark matter sector. Full lines show the total profiles, dashed lines show the corresponding cold dark matter profiles (assumed to follow a Navarro-Frenk-White profile), and dotted lines show the soliton core profile. In the right column, we highlight the scales we use for the weak lensing measurement in white.

where  $\zeta(z) = (18\pi^2 + 82(\Omega_m(z) - 1) - 39(\Omega_m(z) - 1)^2)/\Omega_m(z)$ , which we evaluate with the present day matter density  $\Omega_m(z=0) = 0.3$ . As shown in Fig. 3, smaller ULA particle masses lead to larger cores, which are also larger in lower-mass halos.

For the collisionless part of the profile, we use the Navarro-Frenk-White profile (Navarro et al. 1996), given by

$$\rho_{\text{NFW}}(r) = \frac{\rho_0}{\frac{r}{r_s} \left(1 + \frac{r}{r_s}\right)^2}, \quad (20)$$

with scale radius  $r_s$  and normalisation  $\rho_0$ . We set these values as follows: For a given halo mass and redshift, we compute the radius  $r_{500c}$  using the definition for spherical overdensity masses, and the mean concentration  $c_{500c}$  following the relation by Ragnin et al. (2021). This sets  $r_s = r_{500c}/c_{500c}$ . Using the profile to compute the mass enclosed in  $r_{500c}$ , we set the normalization constant  $\rho_0$  in accordance with Eq. 4 in Navarro et al. (1996) adjusted to the overdensity 500.

We construct the composite model following the recommendations by May & Springel (2023). The transition radius  $r_t$  from a soliton core to the collisionless profiles is defined



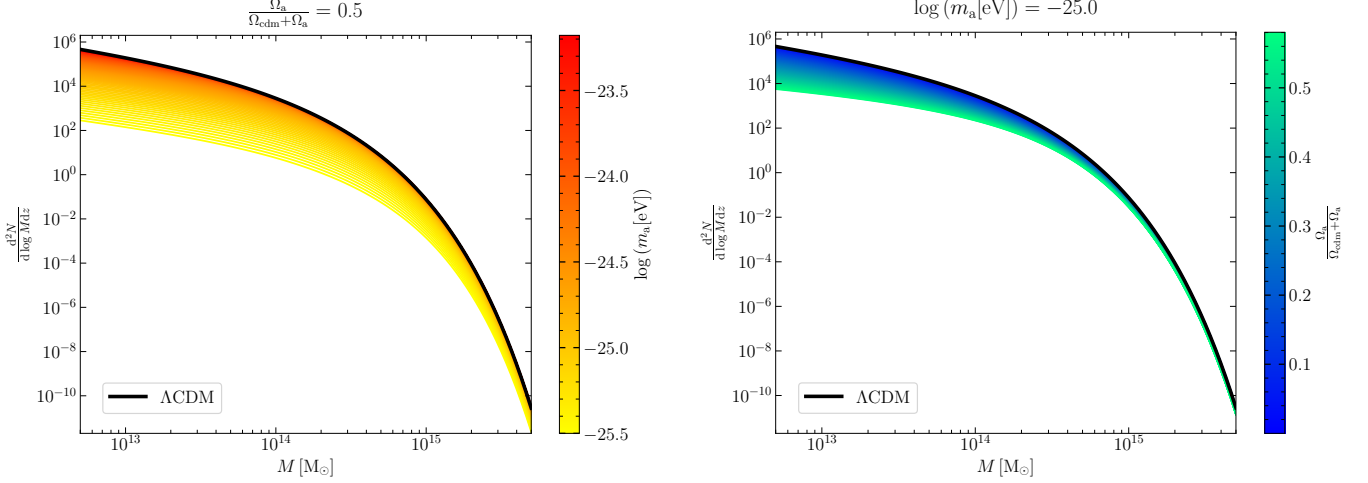


Fig. 4: HMF with [Planck Collaboration et al. \(2020\)](#) cosmological values ( $\Omega_\Lambda \approx 0.7$ ,  $\Omega_m + \Omega_a \approx 0.3$ ) at  $z = 0.1$  with a fixed relative ULA density of  $\Omega_a/(\Omega_{\text{cdm}} + \Omega_a) = 0.5$  and varying ULA mass (left) and a fixed ULA mass of  $m_a = 10^{-25}$  eV and varying ULA abundance (right), compared to the  $\Lambda$ CDM HMF (black). Low mass halo suppression becomes stronger with decreasing ULA mass and increasing ULA abundance. For higher ULA masses of  $m_a \gtrsim 10^{-24}$  eV, the HMF becomes indistinguishable from the one in a  $\Lambda$ CDM cosmology, as is the case for  $\Omega_a \rightarrow 0$ .

by the condition  $\rho_{\text{NFW}}(r_t) = \rho_{\text{sol}}(r_t)$ . If for small ULA masses ( $m_a < 10^{-24}$  eV) no  $r_t$  satisfies this condition, we pick  $r_t = \max(r^2 \rho_{\text{sol}})$ . If there are two solutions, we pick the larger of the two. The total profile is constructed as

$$\rho(r) = \begin{cases} \rho_{\text{sol}}(r) & \text{if } r \leq r_t \\ \rho_{\text{NFW}}(r) & \text{if } r > r_t. \end{cases} \quad (21)$$

[May & Springel \(2023\)](#) discuss that this model is only qualitatively correct for spherically averaged profiles. As such, it is not suited for our precise weak lensing measurements and can only be used to understand the phenomenological effect of ULA particles on massive halo profiles. In the left column of Fig. 3, we show the resulting total mass profiles for different ULA masses  $m_a$  and halo masses  $M$ .

The density profile is not directly observable by the weak gravitational lensing signal, which is sourced by the projected density contrast

$$\Delta\Sigma(R) = \langle \Sigma(< R) \rangle - \Sigma(R), \quad (22)$$

where  $R$  is the 2-dimensional cluster centric distance, and  $\Sigma(R) = \int dz \rho(\sqrt{R^2 + z^2})$ , the projected matter density. The transformation from a 3-dimensional density profile to a density contrast is non-local, as weak lensing depends on the enclosed mass. Flat density profiles thus provide very little signal, while the effect of central overdensity can be observed well outside of their physical extent. These density contrasts are shown in the right panel of Fig. 3.

In this extreme case of a ULA-only dark matter sector, two interesting regimes can be observed. For intermediate ULA masses around  $m_a = 10^{-24}$  eV pronounced soliton cores in the innermost part of the halos appear. Nonetheless, this effect is not observable by our weak lensing measurements, which are restricted to scales around  $\sim 1$  Mpc (highlighted in white in the right panel of Fig. 3). Small ULA particle masses  $m_a \lesssim 10^{-26}$  eV are a second interesting regime. For these ULA masses, cores

become so extended that they dominate the density profile for group-scale halos. At  $m_a \sim 10^{-27}$  eV, also cluster scale halos with  $M < 10^{14} M_\odot$  are dominated by cores. Because of their flat inner profile shape, they provide a vanishing weak lensing signal. Quantitative predictions for the weak lensing signal of groups and clusters would require large-volume hydro-dynamical simulations in ULA cosmology, which are not available to date. We, therefore, conclude that even a pure ULA dark matter sector for  $m_a \gtrsim 10^{-26}$  eV does not significantly impact the prediction for the weak lensing signal of group and cluster scale halos.

In a mixed ULA-cold dark matter model, N-body simulations by [Schwabe et al. \(2020\)](#) show that soliton cores are formed for ULA fractions above  $\Omega_a/(\Omega_m + \Omega_a) \gtrsim 0.1$ . However, below this fraction, these simulations show no evidence for the formation of soliton cores. We conclude that the weak lensing mass calibration remains valid along the full ULA mass range as long as the ULA fraction stays below the aforementioned threshold.

#### 4.5. Mixture model

The eRASS1 cluster catalog contains three classes of objects: galaxy clusters (C), which are of interest, and active galactic nuclei (AGN) as well as background fluctuations misclassified as clusters (NC), the latter two considered contaminants. Our model simultaneously accounts for the cluster counts and the contaminant fractions through the Poisson mixture model, as described in detail in [Kluge et al. \(2024\)](#). The total density is the sum of the three-component model;

$$\lambda_{\text{tot}}(x|\Theta) = \lambda_{\text{C}}(x|\Theta) + \lambda_{\text{AGN}}(x) + \lambda_{\text{NC}}(x). \quad (23)$$

In terms of the total number of objects in each class, we obtain

$$N_{\text{tot}}(\Theta) = N_{\text{C}}(\Theta) + f_{\text{AGN}} N_{\text{tot}}(\Theta) + f_{\text{NC}} N_{\text{tot}}(\Theta), \quad (24)$$

where  $f_{\text{AGN}}$  and  $f_{\text{NC}}$  are the respective fractions of contaminants. Consequently, we can express the number of AGN, false detec-

tions, and the total number of objects in the catalog as a function of the cosmology-dependent number of cluster  $N_C$ :

$$\begin{cases} N_{\text{tot}}(\Theta) = (1/(1 - f_{\text{AGN}} - f_{\text{NC}}))N_C(\Theta) \\ N_{\text{AGN}}(\Theta) = (f_{\text{AGN}}/(1 - f_{\text{AGN}} - f_{\text{NC}}))N_C(\Theta) \\ N_{\text{NC}}(\Theta) = (f_{\text{NC}}/(1 - f_{\text{AGN}} - f_{\text{NC}}))N_C(\Theta) \end{cases} \quad (25)$$

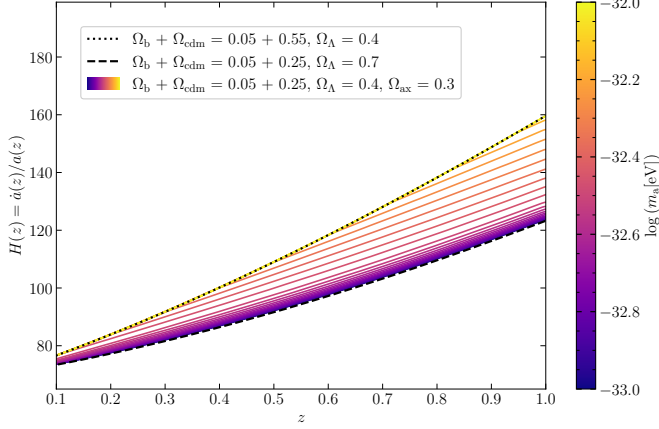


Fig. 5: The Hubble rate  $H(z) = \dot{a}(z)/a(z)$  as a function of redshift. The dotted black line assumes a flat  $\Lambda$ CDM cosmology with  $\Omega_m = 0.6$  and  $\Omega_\Lambda = 0.4$ . The solid black line assumes a flat  $\Lambda$ CDM cosmology with  $\Omega_m = 0.3$  and  $\Omega_\Lambda = 0.7$ . The colored lines represent Hubble rates for an ULA cosmology with fixed relative densities  $\Omega_a = 0.3$ ,  $\Omega_m = 0.3$ , and  $\Omega_\Lambda = 0.4$ . The colored Hubble rates differ only in the ULA mass, as shown by the color bar. This plot demonstrates that ULAs undergo a domain change in the low mass regime between  $\log_{10}(m_a[\text{eV}]) = -32$  and  $\log_{10}(m_a[\text{eV}]) = -33$ . On the low mass end, the Hubble rate approaches the one of a flat  $\Lambda$ CDM cosmology but explains parts of the dark energy component. In the modifications to the pipeline used in G24, we use this accurate Hubble rate extracted from axionCAMB in the distance measure computations.

Starting from the formalism above, we can write the total number of objects as

$$N_{\text{tot}}(\Theta) = \frac{1}{1 - f_{\text{AGN}} - f_{\text{NC}}} \int_x \lambda_C(x|\Theta) dx, \quad (26)$$

and that the number density of contaminants follows  $\lambda_{\text{AGN}}(x|\theta) = N_{\text{AGN}}(\Theta)\mathcal{P}_{\text{AGN}}(x)$ , and  $\lambda_{\text{NC}}(x|\theta) = N_{\text{NC}}(\Theta)\mathcal{P}_{\text{NC}}(x)$ . In this equation,  $\mathcal{P}$  describes the probability distribution function of the respective object, depending on the observables. Finally, the likelihood becomes

$$\begin{aligned} \ln \mathcal{L}(\Theta) = & \sum_i \ln \left( \lambda_C(x_i|\Theta) \right. \\ & \left. + N_{\text{AGN}}(\Theta)\mathcal{P}_{\text{AGN}}(x_i) + N_{\text{NC}}(\Theta)\mathcal{P}_{\text{NC}}(x_i) \right) \\ & - \frac{1}{1 - f_{\text{AGN}} - f_{\text{NC}}} \int_x \lambda_C(x|\Theta) dx. \end{aligned} \quad (27)$$

The contaminant fractions  $f_{\text{AGN}}$  and  $f_{\text{NC}}$  are fitted for during the parameter inference.

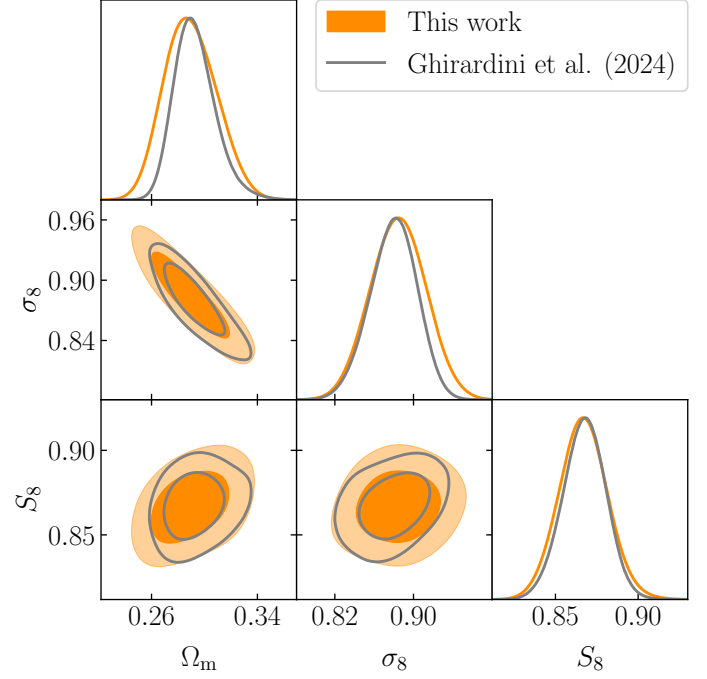


Fig. 6: Consistency check: Posteriors for the cosmological parameters  $\Omega_m$ ,  $\sigma_8$ , and  $S_8$  in the  $\Lambda$ CDM ( $m_a = 10^{-12}$  eV and  $\Omega_a = 10^{-9}$ , these values are chosen arbitrarily such that they satisfy  $m_a \gg 10^{-18}$  eV and  $\Omega_a \ll 10^{-3}$ ). The results are consistent with G24. The inner and outer contour represents the 68% and 95% contour levels respectively.

#### 4.6. Integration of Ultra-light Axions

We introduce ULAs in the cluster abundance cosmological pipeline by implementing a modified version of the power spectrum used to produce the HMF (Diehl & Weller 2021). The HMF is a differential quantity describing the abundance of dark matter halos per unit mass and redshift (see Eq. 8). In the eRASS1 cosmological analysis (G24), the HMF is computed using the *Core Cosmology Library* (pyCCL) (Chisari et al. 2019), which obtains the linear matter power spectrum using the Boltzmann solver CAMB (Lewis & Challinor 2011). In its standard implementation, CAMB does not include ULAs.

In this work, we instead use axionCAMB (Grin et al. 2022), a modified version of CAMB that adds the evolution of primordial density fluctuations caused by an axion field to the Boltzmann solver. The effect of ULAs on the HMF is illustrated in Fig. 4 for different ULA masses  $m_a$  and ULA relic densities  $\Omega_a$ . We use axionCAMB to modify the Hubble rate as a function of redshift  $H(z)$  for a Universe with dark matter composed of ULAs. Using an updated Hubble rate ensures that we properly account for the redshift dependence of the effective properties of ULAs (dark energy or dark matter behavior) when computing the distances between background galaxies and the lens (or the observer) needed for the weak gravitational lensing calibration of the scaling laws as described in Sect. 4.4. Figure 5 shows the influence of ULA mass on the Hubble rate in a cosmology with a high ULA abundance as dark matter. We also use axionCAMB to compute the matter power spectrum. We then compute the r.m.s density fluctuations (Eq. 9) and use it as an input of the multiplicity function  $f(\sigma)$  from Tinker et al. (2008) to compute the halo number density since a precise and accurate fitting function dedicated to ULAs cosmologies is not currently available.

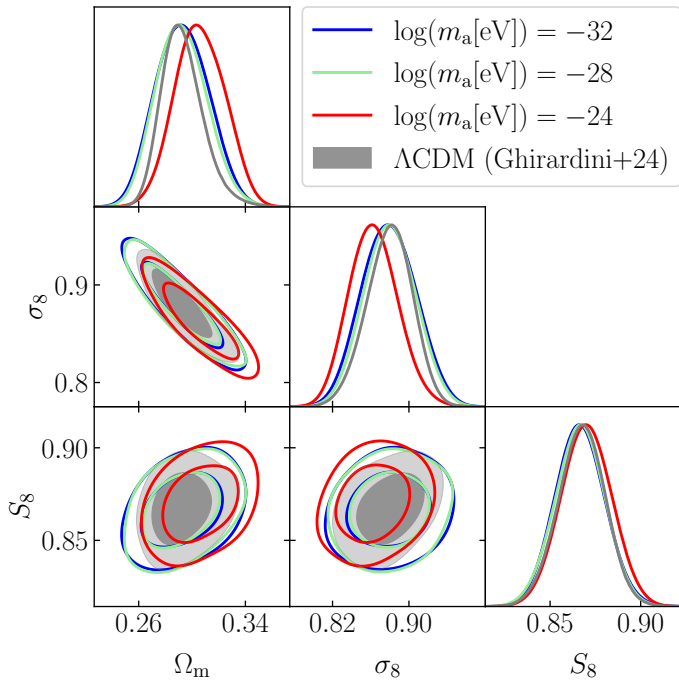


Fig. 7: Posterior distributions for  $\Omega_m$ ,  $\sigma_8$ , and  $S_8$  in a subset of ULA mass bins, representing the full probed ULA mass range. We find consistent cosmological constraints across all mass bins. The results are furthermore compatible with G24. Only the  $m_a = 10^{-25}$  eV mass bin yields deviations from the other bins. The inner and outer contours represent the 68% and 95% contour levels respectively.

This modeling choice is justified by the results of May & Springel (2023), which showed that there is a broad agreement between the HMF measured on their simulations including ULA particles as dark matter and the prediction of a fitting function obtained from a  $\Lambda$ CDM simulation, but using the ULA power spectrum. Additionally, May & Springel (2023) found that current multiplicity functions for ultra-light axions based on the extended Press-Schechter formalism (Du et al. 2017; Kulkarni & Ostriker 2022) actually do not perform as well as the former method.

For ULA masses  $\log_{10}(m_a[\text{eV}]) \lesssim -32.5$ , ULAs undergo the transition between a dark energy-like and a dark matter-like behavior in the redshift range of the eRASS1 galaxy cluster cosmological sample ( $0.1 \leq z \leq 0.8$ ). The ULA mass- and redshift-dependent regime change is illustrated in Fig. 2. Without a theoretically motivated and well-tested model for halo formation subject to such a regime change (essentially the conversion of dark energy-like ULAs into dark matter-like ULAs), we are unable to study this ULA mass range and therefore exclude this regime from our analysis.

However, for ULA masses  $\log_{10}(m_a[\text{eV}]) \gtrsim -32.5$ , we can accurately account for this effect. Above this ULA mass threshold, due to a homogeneous ULA dark matter regime, the halo collapse model is applicable, and only objects at redshifts higher than  $z = 0.8$  (maximum redshift for galaxy clusters in the eRASS1 cosmology sample) are affected by the regime change. This involves the galaxies used for the gravitational weak lensing calibration of the scaling relations (see Sect. 4.4 for details) that extend up to  $z \lesssim 6$  in redshift space. We consider this effect by computing the distances based on the ULA Hubble rate

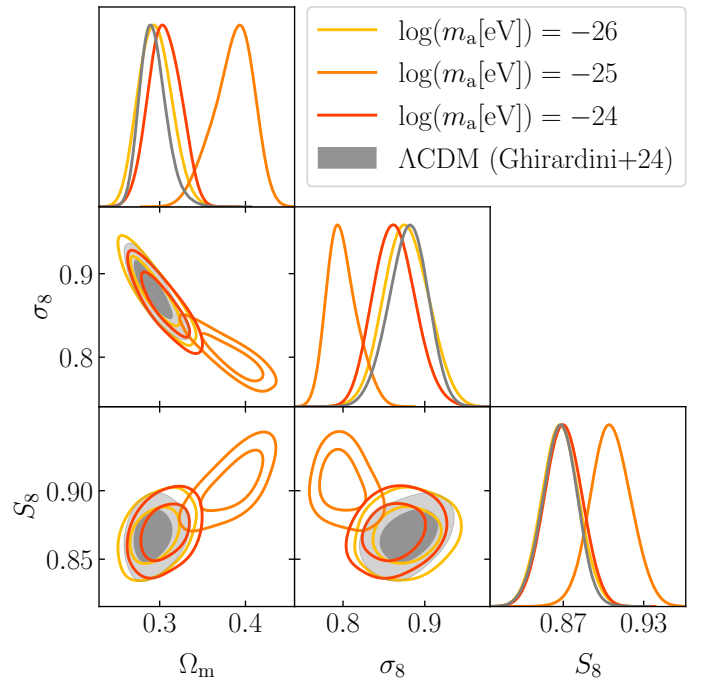


Fig. 8: Posterior distributions for  $\Omega_m$ ,  $\sigma_8$ , and  $S_8$  in the three highest ULA mass bins,  $m_a \in \{10^{-26} \text{ eV}, 10^{-25} \text{ eV}, 10^{-24} \text{ eV}\}$ . While all other mass bins yield consistent results, the constraints in the  $m_a = 10^{-25}$  eV mass bin deviate from the other bin's constraints. We report higher values for both  $\Omega_m$  and  $S_8$ . A similar effect has been reported by Rogers et al. (2023). However, in the context of eRASS1 galaxy cluster number counts, the tension between lower  $S_8$  values from early time probes and higher  $S_8$  values from late time probes is not relieved, as the  $S_8$  values from all other bins as well as the  $\Lambda$ CDM cosmology (G24) already yield a compatible value with early time probes (*Planck* CMB). In the  $m_a = 10^{-25}$  eV mass bin, the  $S_8$  value is higher than the *Planck* CMB value (Planck Collaboration et al. 2020). The authors also note that the deviation could be due to known potential issues with axionCAMB<sup>1</sup>. The inner and outer contours represent the 68% and 95% contour levels respectively.

in this regime. All ULA mass bins above the lowest mass bin are not affected by the regime change, i.e., ULA masses above  $\log_{10}(m_a[\text{eV}]) \lesssim -31.5$  (see Fig. 2 for further details).

Figure 5 illustrates how the regime affects the Hubble rate in a cosmology with a high ULA abundance as a function of ULA mass (color-coded).

## 5. Results and Discussion

In this section, we present the results of the Bayesian inference fitting of cosmological and ULA parameters through galaxy cluster number counts. We use the X-ray count rate, the optical richness, and (where available) the reduced tangential shear profiles given in the eRASS1 galaxy cluster cosmology catalog.

### 5.1. Consistency Checks

We implement several changes to the base cosmological pipeline of G24 as described in detail in Sect. 4. To ensure the adaptations

<sup>1</sup> see <https://github.com/dgrin1/axionCAMB/>

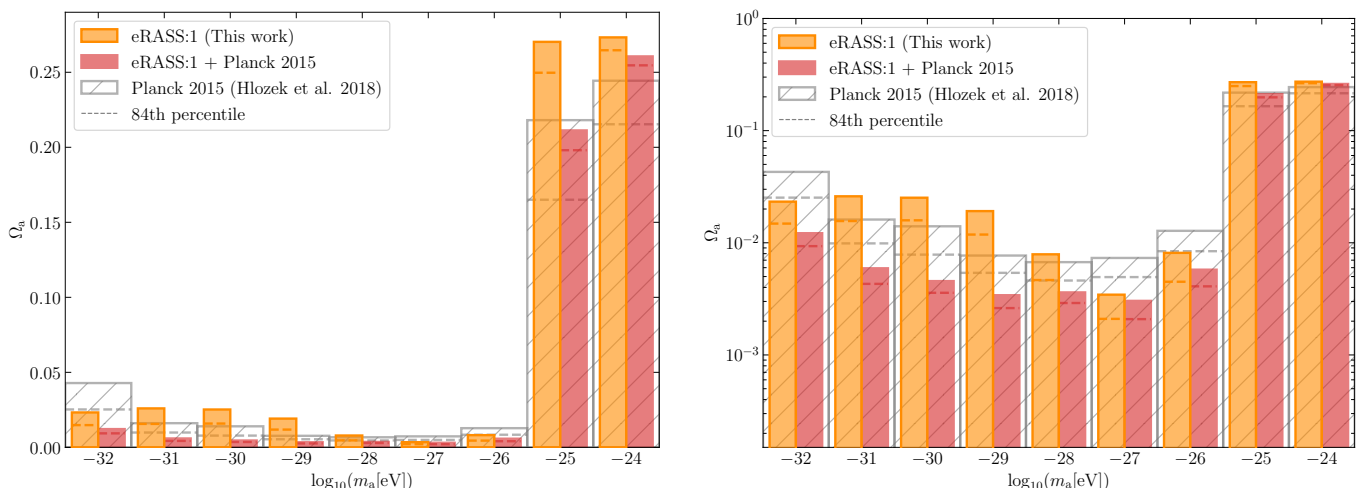


Fig. 9: Upper bounds on the relative ULA density  $\Omega_a$  in each logarithmic ULA mass bin. The left plot shows the upper bounds on  $\Omega_a$  on a linear scale, the right plot on a logarithmic scale. The bar height indicates the 95% confidence interval. The orange bars indicate the bounds obtained by eRASS1 galaxy clusters only, and the gray hatched bars show the bounds obtained from *Planck* 2015 CMB data by Hlozek et al. (2018). The red bars show the bounds obtained from combining the bounds from eRASS1 galaxy clusters with those from *Planck* 2015 CMB data.

Table 1: Cosmological parameters and priors

	Definition	Unit	Priors
$\Omega_m$	Matter density parameter	-	$\mathcal{U}(0.05, 0.95)$
$\Omega_a$	ULAs density parameter	-	$\mathcal{U}(0, 1)$
$\log_{10}(A_s)$	Amplitude of the PS	-	$\mathcal{U}(-10, -8)$
$H_0$	Hubble parameter	$\frac{\text{km}}{\text{s Mpc}}$	$\mathcal{N}(67.77, 0.6)$
$\Omega_b$	Baryon density parameter	-	$\mathcal{U}(0.046, 0.052)$
$n_s$	Spectral index of the PS	-	$\mathcal{U}(0.92, 1.0)$

**Notes.** These priors are used for all the ULA mass bins. For the full set of priors used for the other parameters, including scaling relations and nuisance parameters, see G24. With  $\mathcal{U}(\text{min}, \text{max})$  we indicate a uniform distribution between ‘min’ and ‘max’. With  $\mathcal{N}(\mu, \sigma)$  we indicate a normal distribution centered on  $\mu$  and with standard deviation  $\sigma$ .

do not introduce inconsistencies, we reproduce the main cosmological results in the new ultra-light axion framework by choosing fixed ULA parameters, which are indistinguishable from a  $\Lambda$ CDM cosmology. This limit can be achieved either by setting the ULA relic density to  $\Omega_a = 0$  or for values  $\log_{10}(m_a[\text{eV}]) \gtrsim -18$  (see Fig. 1 and Fig. 4). The code *axionCMB* does only allow positive values for  $\Omega_a$ , so we chose  $\Omega_a = 10^{-9}$ , several orders of magnitude below any other cosmological fluid component in the relevant redshift range. We additionally fix the ULA mass to  $\log_{10}(m_a[\text{eV}]) = -12$ . The matter power spectrum and hence  $\sigma(M, z)$  with this choice of ULA parameters is in perfect agreement with the  $\Lambda$ CDM quantities. We check that running the adapted pipeline leads to almost identical results as compared to the ones obtained in the  $\Lambda$ CDM case shown in G24. A subset of the obtained cosmological parameters is presented in Fig. 6. We conclude that the applied changes did not introduce inconsistencies with the main cosmological results from eRASS1.

## 5.2. Cosmological Constraints

Following the approach developed by Hlozek et al. (2018) and Rogers et al. (2023), we perform a binned analysis in the logarithmic ULA mass  $\log_{10}(m_a[\text{eV}])$ . We consider a total of nine bins, from  $\log_{10}(m_a[\text{eV}]) = -24$  in the highest mass bin to  $\log_{10}(m_a[\text{eV}]) = -32$ . Independent cosmological and scaling relation parameters are considered within each ULA mass bin. The analysis is not sensitive to how the ULA mass is treated within a mass bin, as drawing the ULA mass randomly within a bin or fixing it to the central bin value does not influence the posterior distribution.

We assume a flat ( $\Lambda$ CDM + ULA) cosmology with massless neutrinos to get a conservative estimate of the effect of ULAs. We leave the matter energy density fraction at redshift  $z = 0$ ,  $\Omega_m$ , the baryon energy density fraction at redshift  $z = 0$ ,  $\Omega_b$ , the scalar spectral index,  $n_s$ , the normalization of the matter power spectrum,  $\log(A_s)$ , and the Hubble constant,  $H_0$ , free. We leave the same parameters free for the scaling relations as done in G24. The priors on the cosmological parameters are shown in Table 1.

For all mass bins except the one with  $m = 10^{-25}$  eV, we find no deviations from the  $\Lambda$ CDM cosmological posteriors obtained by G24, and the posteriors are in good agreement between the different ULA mass bins. We show the cosmological posterior distributions for the cosmological parameters  $\Omega_m$ ,  $\sigma_8$ , and  $S_8$  for a subset of ULA mass bins covering the full mass range in Fig. 7.

However, we report a deviation from the  $\Lambda$ CDM cosmological results as well as the other ULA mass bins in the  $m_a = 10^{-25}$  eV range. We find a higher value of  $\Omega_m$  as well as a lower value of  $\sigma_8$ , compared to the other bins as visualized in Fig. 8. A similar effect has been reported by Rogers et al. (2023), when *Planck* 2018 CMB data were used to infer parameters in an ULA cosmology. Rogers et al. (2023) find a lower value for both, the cold dark matter density fraction  $\Omega_c$  and the  $S_8$  value as compared to the other mass bins. Rogers et al. (2023) find a relieved tension between early and late time probe  $S_8$  constraints. We observe a similar effect in the  $m_a = 10^{-25}$  eV mass bin. The authors note that eRASS1 galaxy cluster number counts do not have con-

Table 2: Upper bounds on the ULA relic density ( $\Omega_a$ ) and  $\Omega_a h^2$  at the 95% confidence level in each constraining mass bin for eRASS1 cluster number counts only and when combined with *Planck* 2015 CMB data.

$m_a$	$\Omega_a$		$\Omega_a h^2$	
	(eRASS1)	(eRASS1 + <i>Planck</i> CMB)	(eRASS1)	(eRASS1 + <i>Planck</i> CMB)
$10^{-26}$ eV	< 0.00838	< 0.00576	< 0.00384	< 0.00266
$10^{-27}$ eV	< 0.00357	< 0.00303	< 0.00164	< 0.00139
$10^{-28}$ eV	< 0.00794	< 0.00360	< 0.00361	< 0.00156
$10^{-29}$ eV	< 0.01962	< 0.00336	< 0.00906	< 0.00149
$10^{-30}$ eV	< 0.02616	< 0.00455	< 0.01209	< 0.00202
$10^{-31}$ eV	< 0.02588	< 0.00592	< 0.01196	< 0.00257
$10^{-32}$ eV	< 0.02435	< 0.01214	< 0.01108	< 0.00544

straining power in the ULA parameter space above ULA masses of  $m_a \geq 10^{-26}$  eV. The physical reason for the observed effect is subject to future investigations.

### 5.3. Constraints on the ULA Parameter Space

We find an exclusion region for ULAs by performing a binned analysis, providing upper bounds on the relic density within logarithmic mass bins. Since ULAs form BECs with characteristic extensions given by their thermal de Broglie wavelengths  $\lambda_{dB} \sim 1/m_a$ , ULAs with different masses have imprints on different corresponding scales. ULAs with masses of order  $O(10^{-22}$  eV) have de Broglie wavelengths of order  $O(\text{kpc})$ , while ULAs with masses of order  $O(10^{-33}$  eV) have de Broglie wavelengths comparable to the size of the Universe. As galaxy clusters are probing the  $O(\text{Mpc})$  scales and above, their abundance can constrain ULAs with masses of order  $O(10^{26}$  eV) and below. The inverse relation between scale and ULA mass highlights the importance of galaxy groups in the sample to explore higher ULA mass regimes. Very light ULAs with masses of order  $O(10^{-33}$  eV) mimic a dark energy component, as BECs on the scale of the Universe add a global energy component to the Universe. ULAs with masses slightly above this threshold undergo a transition from an effective dark energy component to an effective dark matter component at some redshift where the size of the Universe exceeds the de Broglie wavelength of the ULA condensate. For this regime, no models exist for halo collapse in the presence of ULAs. Hence, we are not able to probe this region and exclude ULA masses  $\log_{10}(m_a[\text{eV}]) < -32.5$  from our analysis.

We find upper bounds on the ULA relic density  $\Omega_a$  obtained from binning the logarithmic ULA mass with a bin width of  $\Delta \log_{10}(m_a[\text{eV}]) = 1$  around powers of ten. We treat each bin independently. We find upper bounds on the ULA relic density in each ULA mass bin with  $\log_{10}(m_a[\text{eV}]) \leq -26$ , as presented in Fig. 9. We confirm the exclusion region below the  $\log_{10}(m_a[\text{eV}]) = -25$  mass bin, which has been reported by Hložek et al. (2015, 2018), and Rogers et al. (2023). eRASS1 galaxy cluster abundance alone yields the tightest constraints on the ULA relic density in the mass bins  $\log_{10}(m_a[\text{eV}]) \in \{-27, -26\}$  with

$$\begin{aligned} \Omega_a(-26.5 < \log_{10}(m_a[\text{eV}]) \leq -25.5) &< 0.0084, \\ \Omega_a(-27.5 < \log_{10}(m_a[\text{eV}]) \leq -26.5) &< 0.0036, \end{aligned} \quad (28)$$

both at 95% confidence level. Figure 10 shows that these are the tightest upper bounds that have been presented in the literature. Combining our results with *Planck* 2015 CMB data (Hložek et al. 2018), we find even tighter constraints both mass bins:

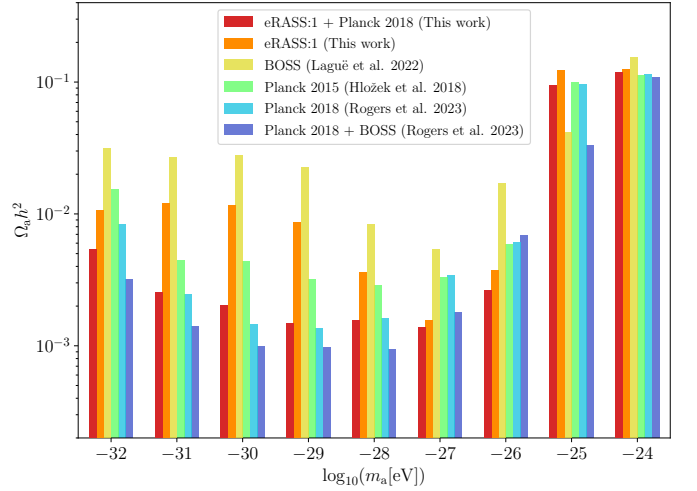


Fig. 10: Comparison of ultra-light axion constraints obtained from eRASS1 galaxy cluster abundance (this work), *Planck* 2015 (Hložek et al. 2018), and 2018 CMB data, BOSS galaxy clustering data (both by Rogers et al. 2023), as well as combined analyses of eRASS1 and *Planck* 2015 (this work) and *Planck* 2018 and BOSS (Rogers et al. 2023). The bar height indicates the 95% exclusion limits of the ULA density  $\Omega_a$  times  $h^2 = (H_0/100)^2$  in each  $\log_{10}(m_a[\text{eV}])$  bin. eRASS1 yields the tightest upper bounds on dark matter ultra-light axions in the  $\log_{10}(m_a[\text{eV}]) \in \{-27, -26\}$  bins.

$$\begin{aligned} \Omega_a(-26.5 < \log_{10}(m_a[\text{eV}]) \leq -25.5) &< 0.0058, \\ \Omega_a(-27.5 < \log_{10}(m_a[\text{eV}]) \leq -26.5) &< 0.0030. \end{aligned} \quad (29)$$

$$(30)$$

From eRASS1 galaxy cluster number counts alone, we find that the ULA relic density  $\Omega_a$  cannot exceed 2.7% of the total energy density of the Universe for  $m_a \leq 10^{-27.5}$  eV and is bound below 0.84% for ULA masses  $10^{-27.5}$  eV  $\leq m_a \leq 10^{-26.5}$  eV and below 0.36% for ULA masses  $10^{-26.5}$  eV  $\leq m_a \leq 10^{-25.5}$  eV. A significant contribution of ULAs to the total dark matter density can thus be ruled out by the growth of structure as observed through eRASS1 galaxy cluster number counts.

It is particularly interesting to compare the eRASS1 cluster number count constraints with those found using BOSS galaxy clustering data as another large-scale structure probe. Rogers et al. (2023) studied the cosmological implications of ULAs

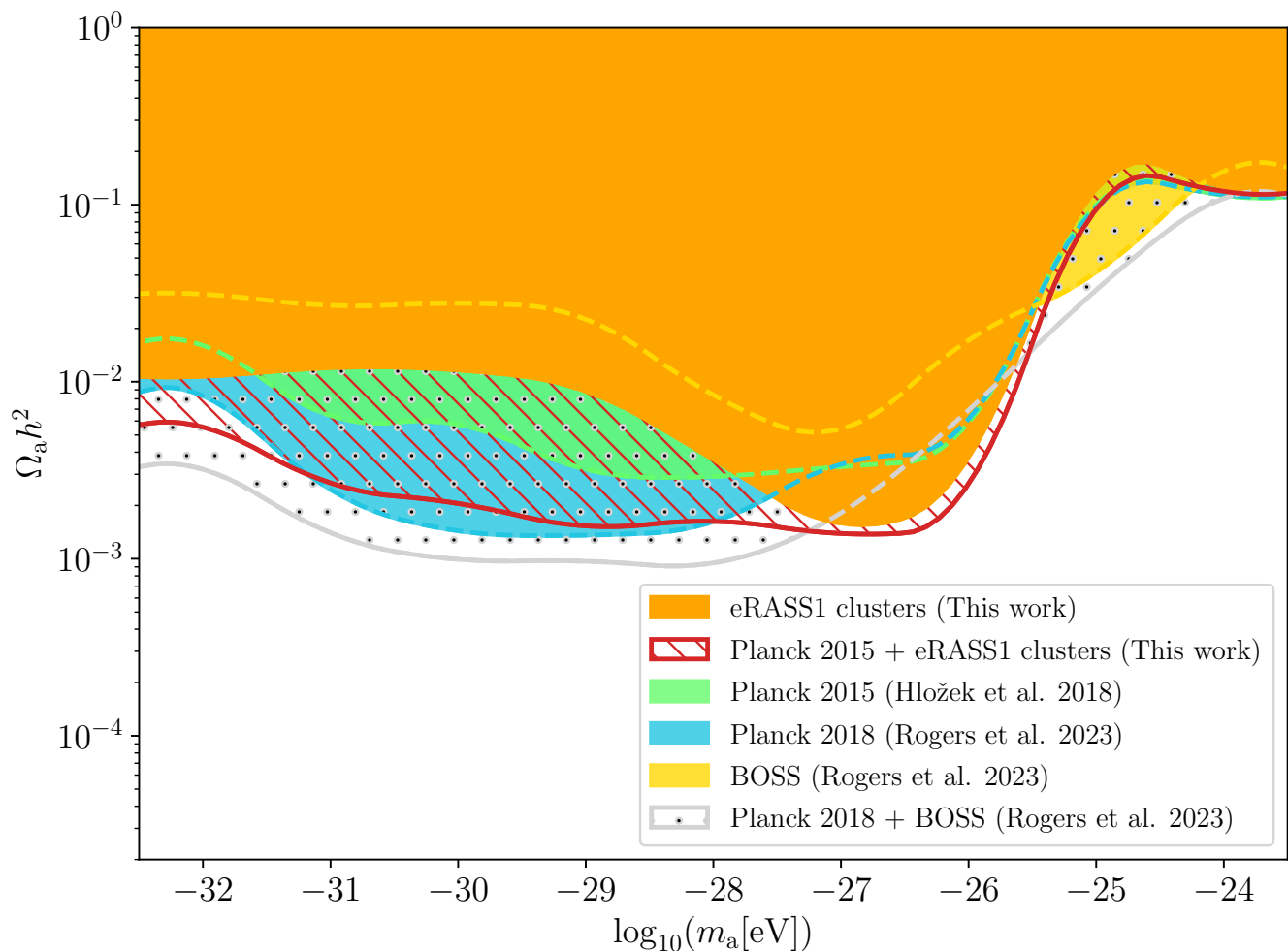


Fig. 11: The 95% confidence level exclusion regions in the  $\log_{10}(m_a[\text{eV}]) - \Omega_a h^2$  space as constrained by different probes. Colored regions represent the part of the parameter space, where one ULA species can be excluded at 95% confidence level, whereas white regions represent the unconstrained parameter space. eRASS1 galaxy cluster number counts (orange) exclude a new region in the parameter space between  $10^{-27.5} \text{ eV} \lesssim m_a \lesssim 10^{-26} \text{ eV}$ , corresponding to galaxy cluster scales. Combining eRASS1 galaxy cluster number counts with the *Planck* 2015 CMB data (red) further improves the eRASS1 bounds on the ULA relic density. For ULA masses below  $m_a \lesssim 10^{-28} \text{ eV}$ , *Planck* 2018 CMB data yields the tightest bounds. Above  $m_a \gtrsim 10^{-25} \text{ eV}$ , galaxy clustering data from BOSS yields the tightest constraints. The curves are interpolated between the central bin values, that represent the 95% confidence levels in the respective bins.

using the twelfth data release of the Baryon Oscillation Spectroscopic Survey (BOSS) catalog (Dawson et al. 2013; Alam et al. 2017) and found upper bounds on the ULA fraction in a binned analysis in the range  $-32 \leq \log_{10}(m_a[\text{eV}]) \leq -26$ . As expected, galaxy clustering and galaxy cluster number counts constrain different ULA mass regimes. This is due to the relation between the ULA mass and the scale it affects: The heavier the ULA, the larger the affected scale in the matter power spectrum, for instance, a ULA with a mass of  $\sim 10^{-24} \text{ eV}$  is only observable on scales below  $\sim 200 \text{ kpc}$ , while a ULA with a mass of  $\sim 10^{-25} \text{ eV}$  is already observable on scales  $\sim 500 \text{ kpc}$  and below (see Fig. 1). While, in comparison to other probes, Rogers et al. (2023) find the tightest constraints ( $\Omega_a h^2 < 0.0418$ ) in the ULA mass bin around  $m_a = 10^{-25} \text{ eV}$ , corresponding to an effect on smaller scales, eRASS1 cluster number counts yield the tightest constraints among complementary in the mass bins  $m_a \in \{10^{-27} \text{ eV}, 10^{-26} \text{ eV}\}$ . ULAs in this mass range af-

fect larger scales, which is constrainable using galaxy cluster number counts. Similar to galaxy clustering data, eRASS1 cluster number counts have reduced constraining power at scales extending the typical probe scales, as seen in the lowest mass bins. On these largest scales (corresponding to ULA masses  $m_a \lesssim 10^{-28} \text{ eV}$ ), CMB measurements by the *Planck* collaboration (Planck Collaboration et al. 2016a, 2020) have the highest constraining power and yield the tightest constraints (Hložek et al. 2015, 2018; Rogers et al. 2023).

For better comparison with the results obtained using other probes (see Fig. 10), we also provide the bounds of each constraining bin for  $\Omega_a$  and  $\Omega_a h^2$  in Table 2.

The authors emphasize that the weak lensing mass calibration as described in Sect. 4.4 remains valid over the full considered ULA mass range as the 95% confidence levels do not exceed ULA fractions of  $\Omega_a / (\Omega_m + \Omega_a) \approx 0.1$  for  $m_a \lesssim 10^{26} \text{ eV}$ . For higher ULA masses, Sect. 4.4 justifies the modeling choice

of keeping NFW profiles for the weak lensing mass calibration up to any ULA fraction.

Our current pipeline is limited by the model of the halo abundance in ULA cosmology, where we use a modified power spectrum in the [Tinker et al. \(2008\)](#) fitting function. Although this is justified by numerical simulations (see Sect. 4.6), our results will be improved if suitable emulators are developed for this model. Additionally, for this pioneering work, we fix the masses of the neutrinos, while the effect of neutrinos is degenerate with ULAs. This modeling choice results in our constraints being conservative upper limits. Including massive neutrinos in the next analyses will significantly tighten our constraints.

## 6. Conclusions

The unique properties of ULAs lead to observable phenomena, such as solitonic cores in dark matter halos and interference patterns on cosmological scales. These features can be probed through astrophysical observations, providing potential evidence for their existence.

Galaxy cluster number counts inferred from the eRASS1 cluster cosmology catalog ([Bulbul et al. 2024](#); [Kluge et al. 2024](#)) can be used to test and constrain the viable dark matter candidates, such as ULAs, through the evolution of the structure growth. Indeed, eRASS1, being the largest ICM-selected sample to date, has a significant constraining power. Additionally, it has the potential to probe the group regime, which is very sensitive to dark matter signatures.

In this work, we perform Bayesian inference on cosmological parameters in a Universe with an additional ULA component parameterized by the logarithmic ULA mass and ULA relic density  $\{\log_{10}(m_a[\text{eV}]), \Omega_a\}$ . The matter power spectrum is computed by `axionCAMB` ([Hložek et al. 2015](#)), from which we compute the HMF using the multiplicity function by [Tinker et al. \(2008\)](#). The forward modeling process requires the selection function developed by [Clerc et al. \(2024\)](#) and additional parameters from the mixture model taking care of possible contaminants, the count-rate-mass scaling relation, and richness-mass scaling relation, calibrated by gravitational weak lensing shear maps ([Grandis et al. 2024](#)). Apart from the adaptations described in Sect. 4.6, we use the framework established in [G24](#) for the parameter inference.

We perform a binned analysis with logarithmic ULA mass bins covering the whole mass spectrum of ultra-light axions from the dark matter regime at  $\log_{10}(m_a[\text{eV}]) = -24$  down to the dark energy regime at  $\log_{10}(m_a[\text{eV}]) = -32$  including an independent full cosmological inference in each bin, assuming a flat Universe. We constrain the following set of cosmological parameters: The matter relic density  $\Omega_m$  and the normalization of the matter power spectrum  $\log(A_s)$ . We leave the Hubble constant  $H_0$ , the scalar spectral index  $n_s$ , and the baryon relic density  $\Omega_b$  free but cannot constrain them as done in [G24](#). We choose a uniform prior on  $\Omega_a$  between 0 and 1 in both scenarios. All common parameters have the same priors as in [G24](#).

We perform a consistency check with the eRASS1 cosmological results from [G24](#) by fixing ULA parameters values to  $\log_{10}(m_a[\text{eV}]) \gg -18$  and  $\Omega_a \rightarrow 0$ , effectively switching off the effect of ULAs on structure growth. The results are consistent with [G24](#), indicating that including ULAs does preserve the correctness and reliability of the inference framework.

The binned analysis of eRASS1 galaxy cluster number counts alone yields tight bounds on the ULA relic density, especially in the two highest ULA mass bins within the exclusion

region  $\log_{10}(m_a[\text{eV}]) \in \{-27, -26\}$ . This ULA mass range corresponds to physical scales (de Broglie wavelengths) of ULA BECs comparable to the typical galaxy cluster scales around 1 Mpc to 10 Mpc. The parameter space excluded by eRASS1 galaxy clusters in comparison to complementary probes is shown in Fig. 11. In the mass range of  $10^{-27.5} \text{ eV} \leq m_a \leq 10^{-26.5} \text{ eV}$ , the upper limit on the ULA relic density is  $\Omega_a < 0.0036$  of the total energy density of the Universe. Similarly, in the mass range of  $10^{-26.5} \text{ eV} \leq m_a \leq 10^{-25.5} \text{ eV}$ , the ULA relic density is constrained to  $\Omega_a < 0.0084$  of the total energy density of the Universe. In the mass regime  $10^{-32.5} \text{ eV} \leq m_a \leq 10^{-27.5} \text{ eV}$ , the ULA relic density is bound below  $\Omega_a < 0.027$ . We conclude that the evolution of structure growth as observed by eRASS1 galaxy cluster number counts rules out ULAs as a significant contribution to the total dark matter density of the Universe. The constraints on the abundance at different confidence levels concerning a logarithmic ULA mass bin are presented in Fig. 9. Overall, these results highlight the potential of cluster abundance measurements and the evolution of the growth of structure as a probe of ULAs. For the first time, we obtain constraints using cluster abundance in a redshift and scale regime complementary to the one probed by other cosmological probes.

In the near future, statistically more powerful cosmological simulations including ULAs (or ultra-light scalar fields, fuzzy dark matter) that predict a HMF model and shear profiles for a sufficiently large cosmological parameter space will be required to provide unbiased constraints. We note that these constraints were obtained using the eRASS1 cosmology sample of 5,259 X-ray-selected massive clusters. The primary sample contains a higher fraction of low-mass objects, so we are more sensitive to ULA signatures, provided that we carefully model the baryonic systematic effects that affect groups. Future analyses of deeper surveys with eROSITA at eRASS:5 depth will provide larger samples of low mass halos with larger constraining power in the ULA parameter space.

*Acknowledgements.* The authors thank Christian Garrel for his contributions to the codebase and the valuable exchange with him. Thanks to Johannes Diehl, Julia Sisk-Reynolds, and Luis A. Ureña-López for the helpful discussions. This work is based on data from eROSITA, the soft X-ray instrument aboard SRG, a joint Russian-German science mission supported by the Russian Space Agency (Roskosmos), in the interests of the Russian Academy of Sciences represented by its Space Research Institute (IKI), and the Deutsches Zentrum für Luft und Raumfahrt (DLR). The SRG spacecraft was built by Lavochkin Association (NPOL) and its subcontractors and is operated by NPOL with support from the Max Planck Institute for Extraterrestrial Physics (MPE). The development and construction of the eROSITA X-ray instrument was led by MPE, with contributions from the Dr. Karl Remeis Observatory Bamberg & ECAP (FAU Erlangen-Nuernberg), the University of Hamburg Observatory, the Leibniz Institute for Astrophysics Potsdam (AIP), and the Institute for Astronomy and Astrophysics of the University of Tübingen, with the support of DLR and the Max Planck Society. The Argelander Institute for Astronomy of the University of Bonn and the Ludwig Maximilians Universität Munich also participated in the science preparation for eROSITA. The eROSITA data shown here were processed using the eSASS software system developed by the German eROSITA consortium. S. Zelmer, E. Bulbul, V. Ghirardini, A. Liu, and X. Zhang acknowledge financial support from the European Research Council (ERC) Consolidator Grant under the European Union’s Horizon 2020 research and innovation program (grant agreement CoG DarkQuest No 101002585). N. Clerc was financially supported by CNES. T. Schrabback and F. Kleinbreil acknowledge support from the German Federal Ministry for Economic Affairs and Energy (BMWi) provided through DLR under projects 50OR2002, 50OR2106, and 50OR2302, as well as the support provided by the Deutsche Forschungsgemeinschaft (DFG, German Research Foundation) under grant 415537506. Marcus Brüggen acknowledges funding by the Deutsche Forschungsgemeinschaft (DFG, German Research Foundation) under Germany’s Excellence Strategy – EXC 2121 “Quantum Universe” – 390833306.

## References

- Abbott, T. M. C., Aguena, M., Alarcon, A., et al. 2022, *Phys. Rev. D*, 105, 023520
- Abbott, T. M. C., Allam, S., Andersen, P., et al. 2019, *ApJ*, 872, L30
- Abel, C., Afach, S., Ayres, N. J., et al. 2020, *Phys. Rev. Lett.*, 124, 081803
- Aihara, H., Arimoto, N., Armstrong, R., et al. 2018, *PASJ*, 70, S4
- Alam, S., Ata, M., Bailey, S., et al. 2017, *MNRAS*, 470, 2617
- Amon, A., Gruen, D., Troxel, M. A., et al. 2022, *Phys. Rev. D*, 105, 023514
- Artis, E., Bulbul, E., Grandis, S., et al. 2024a, arXiv e-prints, arXiv:2410.09499
- Artis, E., Ghirardini, V., Bulbul, E., et al. 2024b, *A&A*, 691, A301
- Arvanitaki, A., Dimopoulos, S., Dubovsky, S., Kaloper, N., & March-Russell, J. 2010a, *Phys. Rev. D*, 81, 123530
- Arvanitaki, A., Dimopoulos, S., Dubovsky, S., Kaloper, N., & March-Russell, J. 2010b, *Phys. Rev. D*, 81, 123530
- Asgari, M., Lin, C.-A., Joachimi, B., et al. 2021, *A&A*, 645, A104
- Bocquet, S., Grandis, S., Bleem, L. E., et al. 2024, arXiv e-prints, arXiv:2401.02075
- Brout, D., Scolnic, D., Popovic, B., et al. 2022, *ApJ*, 938, 110
- Bulbul, E., Liu, A., Kluge, M., et al. 2024, *A&A*, 685, A106
- Bulbul, E., Markevitch, M., Foster, A., et al. 2014, *ApJ*, 789, 13
- Chisari, N. E., Alonso, D., Krause, E., et al. 2019, *CCL: Core Cosmology Library*, Astrophysics Source Code Library, record ascl:1901.003
- Clerc, N., Comparat, J., Seppi, R., et al. 2024, arXiv e-prints, arXiv:2402.08457
- Comparat, J., Eckert, D., Finoguenov, A., et al. 2020, *The Open Journal of Astrophysics*, 3, 13
- Conlon, J. P. 2006, *Journal of High Energy Physics*, 2006, 078
- Conlon, J. P., Day, F., Jennings, N., Krippendorff, S., & Rummel, M. 2017, *J. Cosmology Astropart. Phys.*, 2017, 005
- Costanzi, M., Saro, A., Bocquet, S., et al. 2021, *Phys. Rev. D*, 103, 043522
- Crewther, R. J., di Vecchia, P., Veneziano, G., & Witten, E. 1979, *Physics Letters B*, 88, 123
- Dalal, N. & Kravtsov, A. 2022, *Phys. Rev. D*, 106, 063517
- Dalal, R., Li, X., Nicola, A., et al. 2023, *Phys. Rev. D*, 108, 123519
- Dawson, K. S., Schlegel, D. J., Ahn, C. P., et al. 2013, *AJ*, 145, 10
- de Jong, J. T. A., Verdoes Kleijn, G. A., Kuijken, K. H., & Valentijn, E. A. 2013, *Experimental Astronomy*, 35, 25
- DES Collaboration, Abbott, T. M. C., Acevedo, M., et al. 2024, arXiv e-prints, arXiv:2401.02929
- DESI Collaboration, Adame, A. G., Aguilar, J., et al. 2024, arXiv e-prints, arXiv:2404.03002
- Diehl, J. & Weller, J. 2021, *J. Cosmology Astropart. Phys.*, 2021, 004
- Du, X., Behrens, C., & Niemeyer, J. C. 2017, *MNRAS*, 465, 941
- Fumagalli, A., Saro, A., Borgani, S., et al. 2021, *A&A*, 652, A21
- Gatti, M., Sheldon, E., Amon, A., et al. 2021, *MNRAS*, 504, 4312
- Gendler, N., Marsh, D. J. E., McAllister, L., & Moritz, J. 2024, *J. Cosmology Astropart. Phys.*, 2024, 071
- Ghirardini, V., Bulbul, E., Artis, E., et al. 2024, arXiv e-prints, arXiv:2402.08458
- Giblin, B., Heymans, C., Asgari, M., et al. 2021, *A&A*, 645, A105
- Grandis, S., Bocquet, S., Mohr, J. J., Klein, M., & Dolag, K. 2021, *MNRAS*, 507, 5671
- Grandis, S., Ghirardini, V., Bocquet, S., et al. 2024, arXiv e-prints, arXiv:2402.08455
- Grin, D., Marsh, D. J. E., & Hlozek, R. 2022, *axionCAMB: Modification of the CAMB Boltzmann code*, Astrophysics Source Code Library, record ascl:2203.026
- Hildebrandt, H., van den Busch, J. L., Wright, A. H., et al. 2021, *A&A*, 647, A124
- Hinshaw, G., Larson, D., Komatsu, E., et al. 2013, *ApJS*, 208, 19
- Hložek, R., Grin, D., Marsh, D. J. E., & Ferreira, P. G. 2015, *Phys. Rev. D*, 91, 103512
- Hložek, R., Marsh, D. J. E., & Grin, D. 2018, *MNRAS*, 476, 3063
- Hu, W., Barkana, R., & Gruzinov, A. 2000, *Phys. Rev. Lett.*, 85, 1158
- Hu, W. & Kravtsov, A. V. 2003, *ApJ*, 584, 702
- Hui, L., Ostriker, J. P., Tremaine, S., & Witten, E. 2017, *Phys. Rev. D*, 95, 043541
- Kim, J. E. & Carosi, G. 2010, *Reviews of Modern Physics*, 82, 557
- Kleibreiher, F., Grandis, S., Schrabback, T., et al. 2024, arXiv e-prints, arXiv:2402.08456
- Kluge, M., Comparat, J., Liu, A., et al. 2024, *A&A*, 688, A210
- Kobayashi, T., Murgia, R., De Simone, A., Iršič, V., & Viel, M. 2017, *Phys. Rev. D*, 96, 123514
- Kuijken, K., Heymans, C., Dvornik, A., et al. 2019, *A&A*, 625, A2
- Kulkarni, M. & Ostriker, J. P. 2022, *MNRAS*, 510, 1425
- Laguë, A., Bond, J. R., Hložek, R., et al. 2022, *J. Cosmology Astropart. Phys.*, 2022, 049
- Lesci, G. F., Marulli, F., Moscardini, L., et al. 2022, *A&A*, 659, A88
- Lewis, A. & Challinor, A. 2011, *CAMB: Code for Anisotropies in the Microwave Background*, Astrophysics Source Code Library, record ascl:1102.026
- Li, X., Miyatake, H., Luo, W., et al. 2022, *PASJ*, 74, 421
- Liu, A., Bulbul, E., Ghirardini, V., et al. 2022, *A&A*, 661, A2
- Marsh, D. J. E. 2016, *Phys. Rep.*, 643, 1
- Marsh, D. J. E., Macaulay, E., Trebitsch, M., & Ferreira, P. G. 2012, *Phys. Rev. D*, 85, 103514
- May, S. & Springel, V. 2023, *MNRAS*, 524, 4256
- Merloni, A., Lamer, G., Liu, T., et al. 2024, *A&A*, 682, A34
- Miyatake, H., Sugiyama, S., Takada, M., et al. 2023, *Phys. Rev. D*, 108, 123517
- Navarro, J. F., Frenk, C. S., & White, S. D. M. 1996, *ApJ*, 462, 563
- Nori, M. & Baldi, M. 2018, *MNRAS*, 478, 3935
- Passaglia, S. & Hu, W. 2022, *Phys. Rev. D*, 105, 123529
- Peccei, R. D. & Quinn, H. R. 1977a, *Phys. Rev. D*, 16, 1791
- Peccei, R. D. & Quinn, H. R. 1977b, *Phys. Rev. Lett.*, 38, 1440
- Planck Collaboration, Ade, P. A. R., Aghanim, N., et al. 2016a, *A&A*, 594, A13
- Planck Collaboration, Ade, P. A. R., Aghanim, N., et al. 2016b, *A&A*, 594, A24
- Planck Collaboration, Aghanim, N., Akrami, Y., et al. 2020, *A&A*, 641, A6
- Predehl, P., Andriutschke, R., Arefiev, V., et al. 2021, *A&A*, 647, A1
- Ragagnin, A., Saro, A., Singh, P., & Dolag, K. 2021, *MNRAS*, 500, 5056
- Randall, S. W., Markevitch, M., Clowe, D., Gonzalez, A. H., & Bradač, M. 2008, *ApJ*, 679, 1173
- Reynolds, C. S., Marsh, M. C. D., Russell, H. R., et al. 2020, *ApJ*, 890, 59
- Rogers, K. K., Hložek, R., Laguë, A., et al. 2023, *J. Cosmology Astropart. Phys.*, 2023, 023
- Rogers, K. K. & Peiris, H. V. 2021, *Phys. Rev. Lett.*, 126, 071302
- Schive, H.-Y., Chiueh, T., & Broadhurst, T. 2014, *Nature Physics*, 10, 496
- Schwabe, B., Gosenca, M., Behrens, C., Niemeyer, J. C., & Easther, R. 2020, *Phys. Rev. D*, 102, 083518
- Scolnic, D., Brout, D., Carr, A., et al. 2022, *ApJ*, 938, 113
- Seppi, R., Comparat, J., Bulbul, E., et al. 2022, *A&A*, 665, A78
- Sevilla-Noarbe, I., Bechtol, K., Carrasco Kind, M., et al. 2021, *ApJS*, 254, 24
- Stott, M. J. & Marsh, D. J. E. 2018, *Phys. Rev. D*, 98, 083006
- Sunyaev, R., Arefiev, V., Babyshkin, V., et al. 2021, *A&A*, 656, A132
- Svrcek, P. & Witten, E. 2006, *Journal of High Energy Physics*, 2006, 051
- Tinker, J., Kravtsov, A. V., Klypin, A., et al. 2008, *ApJ*, 688, 709
- Vogt, S. M. L., Marsh, D. J. E., & Laguë, A. 2023, *Phys. Rev. D*, 107, 063526
- Winch, H., Rogers, K. K., Hložek, R., & Marsh, D. J. E. 2024, arXiv e-prints, arXiv:2404.11071
- Wright, A. H., Hildebrandt, H., van den Busch, J. L., & Heymans, C. 2020, *A&A*, 637, A100
- Zhao, C., Variu, A., He, M., et al. 2022, *MNRAS*, 511, 5492